Tampere University

Arttu Hietalahti

WIDE SPECTRAL CALIBRATION FOR III-V MULTI-JUNCTION SOLAR CELL RESEARCH

Faculty of Engineering and Natural Sciences
Master of Science Thesis
February 2023

ABSTRACT

Arttu Hietalahti: Wide spectral calibration for III-V multi-junction solar cell research
Master of Science Thesis
Tampere University
Science and Engineering
February 2023

Multi-junction solar cells (MJSC) are a modern photovoltaic technology which currently have the highest power conversion efficiencies of any solar cells. Their high efficiency is due to their unique way of capturing the incident solar optical energy in many spectrally optimized subcells. MJSC's are currently mostly used in space applications due to their high cost-per-watt. As the technology matures towards better cost-efficiency, MJSC's have been projected to gain popularity also in terrestrial applications such as concentrated photovoltaic power plants and small devices like drones, for example.

The aim of this thesis is to create and test a new calibration method for solar simulators. This method is optimized for MJSC research by allowing accurate calibration over a wide wavelength spectrum. The accuracy of the calibration has become increasingly important when the number of MJSC subcells has increased. The ultimate purpose of this new calibration method is to support the quality and progress of MJSC research by allowing more accurate characterization results. The novelty in this method is the use of outside measurements under illumination of the real Sun, with the corresponding local simulated spectra being used in the calibration data analysis.

The outside measurements were performed in Tampere, Finland during summer 2022. The outside measurement data was analyzed and converted to calibration targets that were then used in calibration of two solar simulators. The calibration current density targets were successfully reached within 1% error margin for the AM1.5D standard spectrum in the range from 300 nm to 1600 nm by using a LED-based multiband solar simulator. As a side result, the calibration of the LED simulator was also performed for the AM1.5G and AM0 spectra with an accuracy of roughly 2% and 6% for the calibration current density, respectively. The same calibrations were performed on a Xenon arc solar simulator, resulting in significantly higher error margins of up to 58% which was an expected result. This result emphasizes the importance of choosing a suitable solar simulator to apply the calibration method.

Overall, the research was successful and the calibration method proved to be a good alternative to the other commonly used methods, with its main benefits including accuracy, spectral width, and cost-effectiveness. The calibration tests demonstrate that the method is particularly well suitable for use with LED-based solar simulators. It can be concluded that the final accuracy of the method is within 5-10% for the AM1.5D and AM1.5G spectra, fitting well within the A-class spectral mismatch specification which was the target of this thesis. Future interests for this research could include further cross-comparison with other calibration methods, testing with a larger selection of different samples, and further improving the accuracy of the simulated solar spectrum.

Keywords: solar cell calibration, multi-junction solar cell, solar radiation, solar simulation

TIIVISTELMÄ

Arttu Hietalahti: Laaja spektrikalibraatio III-V moniliitosaurinkokennojen tutkimukseen
Diplomityö
Tampereen yliopisto
Teknis-luonnontieteellinen
Helmikuu 2023

Moniliitosaurinkokennot ovat tärkeä moderni teknologia aurinkosähkön alalla. Niillä on korkeimmat tehokonversion hyötysuhteet kaikista aurinkokennoteknologioista. Korkea hyötysuhde johtuu moniliitosaurinkokennojen ainutlaatuisesta tavasta hyödyntää auringon spektrin optinen teho monessa eri alikennossa, jotka ovat optimoitu spektrin eri aallonpituusalueille. Korkean hintansa vuoksi moniliitosaurinkokennojen käyttö keskittyy pääasiassa avaruusteknologiaan. Moniliitosteknologia kuitenkin kehittyy jatkuvasti kohti parempaa hinta-tehosuhdetta, ja niiden käyttöasteen ennustetaan kasvavan myös maanpäällisissä sovelluksissa. Mahdollisia maanpäällisiä sovelluksia moniliitosaurinkokennoille ovat esimerkiksi konsentroidun valon aurinkosähkövoimalat sekä pienet autonomiset laitteet kuten drone-lennokit.

Tämän työn tarkoituksena on kehittää ja testata uusi kalibraatiomenetelmä aurinkosimulaattoreille. Menetelmä on optimoitu moniliitosaurinkokennojen tutkimukseen, jossa tarvitaan erityisen tarkka spektrikalibraatio laajalla aallonpituusalueella. Moniliitosaurinkokennojen tutkimuksessa on havaittu spektrikalibraation tarkkuuden olevan yhä tärkeämpää kun liitosten määrää lisätään aurinkokennossa. Työllä pyritään tukemaan tutkimuksen laatua ja edistymistä mahdollistamalla tarkempia mittaustuloksia moniliitosaurinkokennoille. Menetelmän uutuustekijänä on oikean auringon hyödyntäminen ulkokalibraatiomittauksissa sekä paikallisen simuloidun spektrin käyttäminen kalibraation laskennassa.

Ulkokalibraatiomittaukset suoritettiin ulkona Tampereella kesän 2022 aikana. Mittaustuloksista saatiin menetelmän analyysikeinojen avulla laskettua virrantiheyden kalibraatioarvot, joita käytettiin kahden eri aurinkosimulaattorin kalibrointiin. AM1.5D-standardispektrin kalibraatiossa virrantiheyden kalibraatioarvot saavutettiin alle 1%:n virhemarginaalilla aallonpituusvälillä 300 - 1600 nanometriä, kun käytössä oli LED-teknologiaan perustuva monikaistainen aurinkosimulaattori. Sivutuloksena suoritettiin myös spektrikalibraatiot AM1.5G- ja AM0-standardispektreille, joille virrantiheyden kalibraatioarvon virhemarginaali oli noin 2% ja 6% vastaavasti. Samat spektrikalibraatiot suoritettiin myös toiselle aurinkosimulaattorille, jonka valonlähteenä on ksenon-kaarilamppu. Odotetun mukaisesti ksenon-aurinkosimulaattorilla kalibraation tarkkuus oli huomattavasti huonompi kuin LED-aurinkosimulaattorilla, ja virhemarginaali oli jopa 58 prosenttia. Tämä tulos korostaa aurinkosimulaattorin tyyppivalinnan ja erityisesti spektrin säädettävyyden tärkeyttä kalibraatiomenetelmän käytössä.

Kokonaisuudessaan tutkimus onnistui hyvin ja kalibraatiomenetelmä saatiin täyttämään sille asetetut vaatimukset. Menetelmä on uusi vaihtoehto spektrikalibraatiolle ja muihin menetelmiin verrattuna sen etuina ovat tarkkuus, aallonpituuskaistan leveys sekä kustannustehokkuus. Kalibraatiotestit osoittivat että menetelmä toimii erityisen hyvin LED-teknologiaan perustuvien aurinkosimulaattoreiden kanssa, sillä niiden laaja spektrisäädettävyys mahdollistaa kalibraatioarvojen saavuttamisen hyvin tarkasti. Kun kaikki virhelähteet sekä ulkomittauksissa, kalibraatiolaskennassa, sekä kalibrointitesteissä otetaan huomioon, menetelmän kalibraatiotarkkuuden arvioidaan olevan noin 5-10% AM1.5D- ja AM1.5G-standardispektreille. Tämä tarkkuus ylittää standardissa määritetyn A-luokan spektrikalibraation vaatimukset, mikä oli asetettu tämän työn tavoitteeksi. Seuraavat tutkimusvaiheet kalibraatiomenetelmälle voisivat sisältää laajemman vertailun muita kalibraatiomenetelmiä vastaan, kalibraationäytteiden lukumäärän lisäämisen, sekä paikallisen spektrisimulaation tarkkuuden hienosäätämisen.

Avainsanat: aurinkokennojen kalibraatio, moniliitosaurinkokenno, auringon säteily, auringon simulaatio

Tämän julkaisun alkuperäisyys on tarkastettu Turnitin OriginalityCheck -ohjelmalla.

PREFACE

This work was carried out at the Optoelectronics Research Centre (ORC) of Tampere University. Funding was provided by the AMETIST project (ERC 695116) and the Fortum and Neste Foundation.

First I would like to express my gratitude to my supervisor Dr. Arto Aho, who initially granted me with the opportunity of working at ORC in 2019 and has been guiding me through the first years of my scientific career. He has provided me with the freedom of testing my own ideas in the laboratory while always being available for support when a more experienced opinion is needed. Second acknowledgement goes to Prof. Mircea Guina, who has similarly trusted my work and has always supported me in many challenges along the road. I also thank Prof. Anders Lindfors from the Finnish Meteorological Institute for performing the spectral simulations for this thesis, as well as providing his expertise in atmospheric physics and radiative transfer.

ORC has been a great place to start my career in physics thanks to the open, friendly and innovative people at ORC. From the solar cell team, I would like to thank Dr. Antti Tukiainen for his help in all things related to laboratory instruments. Thanks to Dr. Jarno Reuna for being a great office mate for many years. My gratitude also goes towards my closest colleagues in the solar cell team: Riku, Elina, Veikka, Antti F., Seela, Juuso, Timo and Marianna. I have had so many fun experiences working in the lab with you all. Thanks to many other people from ORC for the good working atmosphere and fun open conversations in the coffee room.

Personally, I would like to thank my family and friends for supporting me during my studies. Most importantly, their company has been a powerful antidote for the stress I have encountered at times. Cheers to the many fun experiences in the past and in the future. Final thanks goes to my dear partner Anniina, who has been my most important supporter during this thesis.

In Tampere, 28th February 2023

Arttu Hietalahti

CONTENTS

LIST OF SYMBOLS AND ABBREVIATIONS

1J	single-junction solar cell
2J	two-junction solar cell
4J	four-junction solar cell
III-V	atomic groups III and V of the periodic table
AM	Air Mass
AM0	"Air Mass 0" extraterrestrial solar spectrum standard (ASTM E-490)
AM1.5D	"Air Mass 1.5" direct terrestrial solar spectrum standard (ASTM G173-03)
AM1.5G	"Air Mass 1.5" global terrestrial solar spectrum standard (ASTM G173-03)
CPV	concentrated photovoltaics
EQE	external quantum efficiency
FF	fill factor
FMI	Finnish Meteorological Institute
FS	fused silica
GWp	peak Gigawatts
IR	infrared
IV	current-voltage
LED	light-emitting diode
MJSC	multi-junction solar cell
MPP	maximum power point
ORC	Optoelectronics Research Centre, Tampere University
PV	photovoltaics
RT	radiative transfer
RTE	radiative transfer equation
SZA	solar zenith angle
TPW	total precipitable water
TWp	peak Terawatts
UTC	universal coordinated time

UV	ultraviolet
A	solar cell area
E_g	band gap energy
E_{phot}	photon energy
η	power conversion efficiency
I_0	dark saturation current
I_{dark}	dark current (no incident illumination)
I_i	subcell current
I_{phot}	photocurrent (under incident illumination)
I_{sc}	short-circuit current
J_{sc}	short-circuit current density
k	Boltzmann constant
λ	wavelength
n	ideality factor
P	power
P_{max}	maximum power
$\Phi_{in}(\lambda)$	incident spectral photon flux
q	elementary charge
T	temperature
V	voltage
V_i	subcell voltage
V_{oc}	open-circuit voltage

1 INTRODUCTION

Photovoltaics (PV) is the technology of converting sunlight into electricity. Solar cells and panels are arguably the most important PV devices due to their major role in the global energy production. The first practical silicon solar modules started being introduced in the 1950's, with the first devices being extremely expensive, mostly restricting their use into space satellites and probes [1]. Solar cells have since been under development towards higher efficiency, lower cost, and better stability. In the 2000's, the technology had matured enough that global PV installations started increasing near exponentially, a trend which still continues today with a record of 175 GWp (peak Gigawatts) being installed in 2021 [2]. Global PV capacity reached 1 TWp in 2022 [3], and is projectd to reach 2 TWp by 2026 [4]. PV research funding has also increased massively due to the increased global interest in employing green energy sources to combat climate change [2] [5]. While silicon solar cells continue to dominate with over 90% share of the global PV capacity, many other solar cell technologies have been introduced for many different applications where traditional silicon cells are considered sub-optimal.

Multi-junction solar cells (MJSC) are an important modern PV technology. Their main benefit is their extremely high conversion efficiency which is realized by capturing different parts of the solar radiation spectrum in different layers, called subcells. Each subcell is optimized to capture their portion of the solar radiation spectrum, resulting in a very efficient utilization of the energy contained in the whole wavelength range. For comparison, the conversion efficiency record for silicon solar cells is 26.6% [6] while the highest solar cell efficiency is 47.6% which was measured from a MJSC with four junctions under concentrated sunlight [7]. Though their efficiency is already high in standard one-sun illumination conditions, MJSC's often reach their maximum efficiency under concentrated sunlight through optics. Therefore, many of the new applications of MJSC's are in concentrated photovoltaics (CPV), which potentially allows for significantly reduced system costs because of the very small cell size that is required [8]. MJSC's have still relatively high cost-per-watt compared to other technologies, which is why their global installation capacity remains miniscule[8]. Their main applications are currently in space technologies, with some applications emerging in small terrestrial devices such as drones. [9] However, MJSC's are still under joint global development effort towards lower cost-per-watt, with some projections aiming for increased terrestrial CPV installations in the next decades [10] [9].

Characterization of solar cells is an important part of photovoltaic research. In the lab-

oratory, solar cells are measured under illumination from a solar simulator, which is a device that is designed to mimic the solar irradiation spectrum. Solar simulators allow for repeatable, standardized and time-independent measurements when compared to measurements under the real Sun. Spectral calibration of the solar simulator is essential for the accuracy and reliability of the measurements performed with it. MJSC's are extremely sensitive to spectral variations, which is why the calibration accuracy is critically important in MJSC research. The highest calibration standard for solar simulators, class A ([11], allows for up to $\pm$ 25% mismatch in the spectrum in each wavelength sub-band. Such mismatch can result in an inaccuracy of more than 25% in the MJSC measurement, producing unreliable results which can lead to many difficulties in the research process. In the solar cell research group at ORC, the solar simulator calibration accuracy has become critically important as research has progressed towards an increased number of subcells for the MJSCs.

In this thesis, a new method for calibrating a solar simulator for MJSC research is introduced. The method is based on outside measurements from which the calibration data is calculated. Simulated local solar spectra are used in the calculation to analyze and make corrections for the spectral mismatch, which describes the differences in spectral photon flux between the local spectrum and the standard spectrum. The calibration data is then used to calibrate a LED-based solar simulator with the target of less than 10% spectral mismatch for the AM1.5D standard spectrum, which is a big improvement over the A-class standard of up to 25% mismatch. The benefits of this new calibration method include accuracy, cost-effectiveness and scalability across many different samples. The calibration method is tailored to fulfill the requirements of MJSC research at ORC by accurately calibrating for a wide spectral range from 300 to 1600 nanometers. The main calibration target spectrum of this thesis is the AM1.5D direct standard spectrum (ASTM G173-03 [12]), with also the AM1.5G (ASTM G173-03) and AM0 (ASTM E-490 [13]) spectra being calibrated as a side result.

In Chapter 2, the theory behind solar radiation, solar simulators, and solar cells is introduced. In Chapter 3, the calibration method is introduced, after which the results are presented and discussed. Chapter 4 contains a summary of the thesis research.

2 THEORY

In this Chapter, the theory behind the thesis research is introduced. Section 2.1 covers the basics of solar radiation and how it can be computationally simulated. In Section 2.2, solar simulators are discussed briefly, with emphasis on the related standards and simulator types. Section 2.3 contains a brief introduction of the structure and operation principle of semiconductor solar cells, continuing with their performance characteristics. Section 2.4 briefly covers the theory behind multi-junction solar cells.

2.1 Solar radiation

Solar cells generate power from sunlight which is the electromagnetic radiation of the Sun. They are optimized to produce maximum power in their target application, whether it is in terrestrial solar power plants or in space satellites where the incident spectrum can be very different. [14] In order to develop high-efficiency solar cells, it is critical to understand the basic characteristics of solar radiation which are discussed in this Section.

2.1.1 The solar irradiance spectrum

The Sun is the star located at the center of our Solar System. It is composed of hot plasma which emits incandescent blackbody radiation, with the heat being generated by nuclear fusion in the core [15]. Its emitted irradiance spectrum, that is the electromagnetic energy distribution over the wavelength range, is well approximated with the spectrum of an ideal blackbody object at T $\approx$ 5800 K by Planck's law. Though the solar spectrum matches the blackbody spectrum quite well, there are some differences mainly at ultraviolet (UV) and visible wavelengths below 700 nm due to numerous absorption and emission solar lines. [16]

The irradiance of solar radiation, that is the optical power per unit area, is proportional to the inverse square of the distance. At Earth's mean distance from the Sun, which is one Astronomical Unit (AU) i.e. 150 million kilometres [15], the mean irradiance spectrum in vacuum of space is described by the Air Mass 0 (AM0) standard (ASTM E-490 [13]). The AM0 standard spectrum has a total irradiance of $1366 \frac{W}{m^2}$ [13]. It is often used as reference in research of solar cells for extraterrestrial applications in satellites, for example.

When solar radiation enters the Earth's atmosphere, its spectrum changes due to attenuation by many different scattering and absorption processes [16]. The total attenuation

of the spectrum is dependent on the effective distance that the light travels through the atmosphere, which is described by the Air Mass (AM) factor. The AM factor can be approximated by equation [17]

$$AM = \frac{1}{cos(\theta_z)}, \tag{2.1}$$

where θ_z is the solar zenith angle (SZA), that is the angle between the Sun and the ground vertical. This simple equation produces satisfactory results for small values of SZA, however for accurate spectral calculations, more involved equations are used which also consider the curvature of the Earth [18].

In order to facilitate standardized photovoltaic (PV) research results, there has been a need for establishing standardized solar spectra for terrestrial illumination. The two most important terrestrial solar spectrum standards are the AM1.5G and AM1.5D spectra, which are based on long-term data from a sunlight measurement network in the United States [14] [19]. In both spectra, the SZA is roughly 48° which corresponds to AM1.5 by Equation 2.1.

AM1.5D ("Direct") spectrum includes only the direct radiation from the sun with a 5.8° angular aperture. The total irradiance of AM1.5D spectrum is $900\frac{W}{m^2}$, however for convenience it is often normalized to $1000\frac{W}{m^2}$ [20]. It is the go-to standard in research of concentrated photovoltaics (CPV) where the direct sunlight is focused to the solar cell with optics. The current active standard for the AM1.5D spectrum is the ASTM G173-03 standard. [12]

The AM1.5G spectrum also includes diffuse radiation from all around the sun, i.e. from the blue sky, in addition to the direct radiation, making the total irradiance slightly higher at $1000\frac{W}{m^2}$. It is therefore most useful in research of flat panel solar cells whose light acceptance angle extends to most of the sky. [20] The currently active standard for the AM1.5G spectrum is the ASTM G173-03 standard [12].

The AM0, AM1.5D and AM1.5G standard solar spectra are plotted in Figure 2.1.

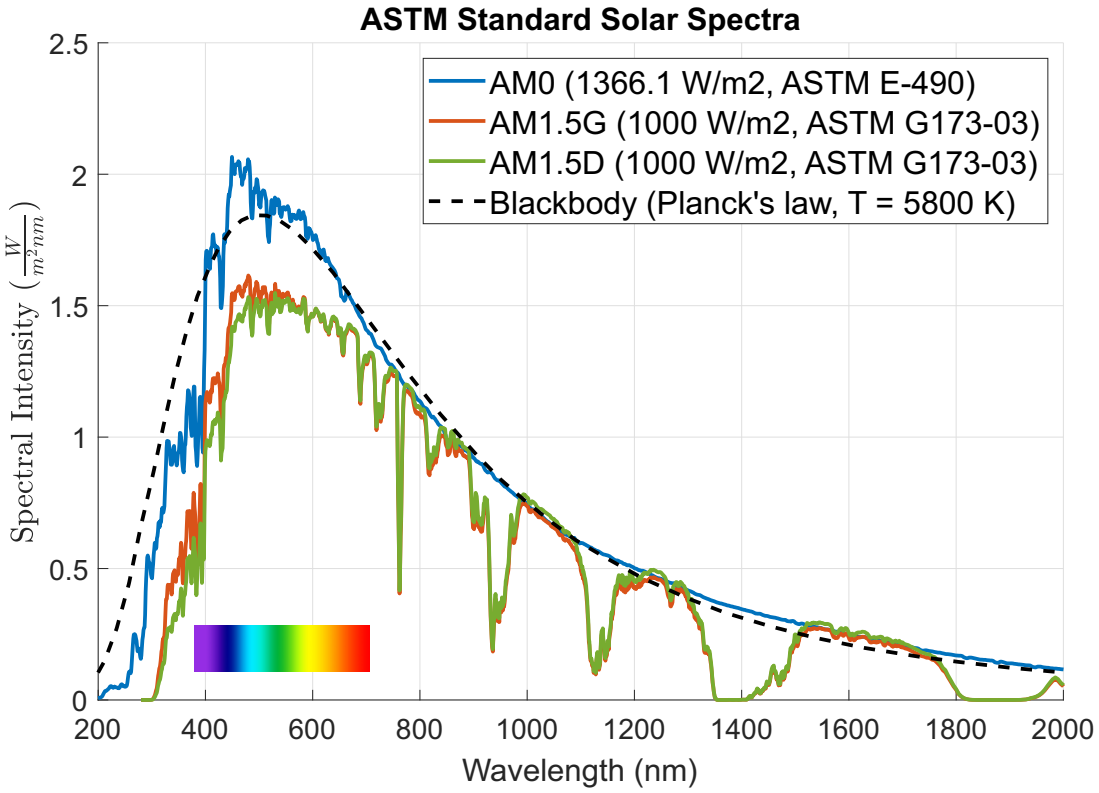

Figure 2.1. *AM0, AM1.5G and AM1.5D standard solar spectra. Included blackbody spectrum at T = 5800 K for reference. AM1.5D spectrum is normalized to total irradiance of* $1000\frac{W}{m^2}$ *for convenience.*

Figure 2.1 shows the main differences between the three standard solar spectra. The AM0 extraterrestrial spectrum has the highest overall irradiance and matches the blackbody approximation quite closely. The terrestrial AM1.5D and AM1.5G spectra are attenuated by the atmosphere, which reduces the overall irradiance and creates multiple local irradiance drops at wavelength bands of high absorption and scattering [16]. When the AM1.5D and AM1.5G spectra are both normalized to a total irradiance of $1000\frac{W}{m^2}$, they have a very similar shape but with slight differences. The AM1.5G spectrum has slightly more irradiance in the ultraviolet and visible ranges below 600 nm, while the AM1.5D spectrum has slightly more irradiance in the infrared range above 700 nm.

Different components of terrestrial solar radiation and atmospheric effects are illustrated in Figure 2.2. Most important is the distinction between the direct irradiance and diffuse irradiance. The direct irradiance accounts for a small "disc" around the sun, with a full aperture angle of 5.8°. The diffuse irradiance contains all the remaining irradiance from the sky around the disc. Both the direct and diffuse irradiance are affected by many factors, which are discussed in the next Sections.

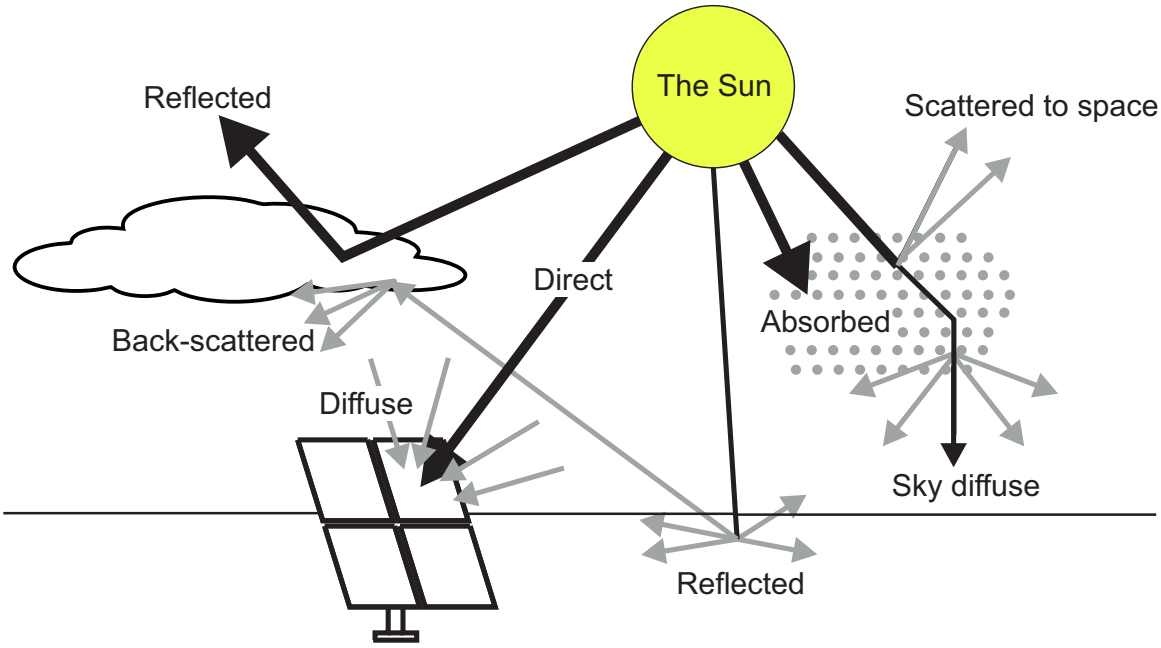

Figure 2.2. *Terrestrial solar radiation and atmospheric effects.*

2.1.2 Factors affecting solar irradiance

The most important factor affecting the terrestrial solar irradiance spectrum is the solar zenith angle (SZA). The irradiance has an inverse relation to the SZA, and the maximum irradiance is achieved when sun is at its highest point which corresponds to minimum SZA. This inverse relation is explained by the increased attenuation of radiation by scattering and absorption when it travels through longer distances in the atmosphere. [16] This relation is illustrated in Figure 2.3, which includes the simulated terrestrial solar spectrum at different times on a typical cloudless June day in Tampere, Finland.

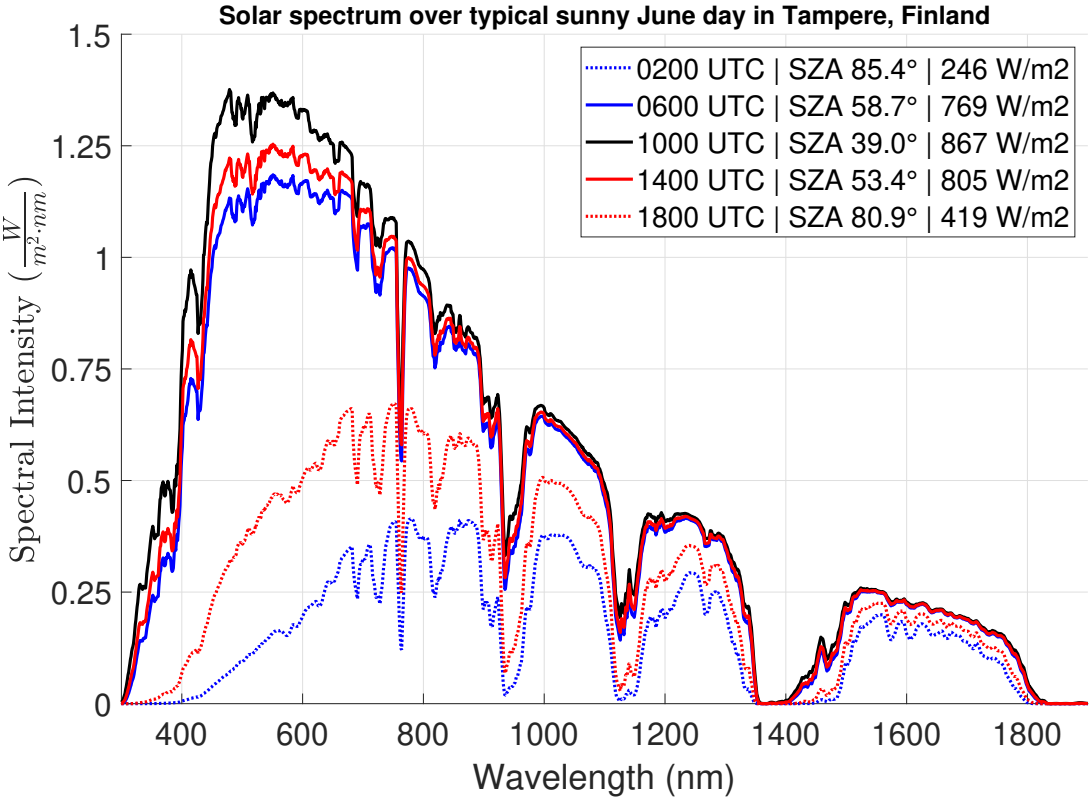

Figure 2.3. *The simulated solar spectrum over a typical cloudless June day in Tampere, Finland. Black line (10:00 UTC) corresponds to mid-day sun with minimum SZA and highest irradiance.*

From Figure 2.3, it is clear that the SZA greatly affects the irradiance across the whole spectrum. The irradiance is highest at noon (10:00 UTC), and it is decreased when moving further away from mid-day hours. The relative irradiance change through the day is inversely proportional to the wavelength: the shorter wavelengths are greatly attenuated when the sun is closer to the horizon (larger SZA), while at longer wavelengths the attenuation related to SZA is more subtle. This is the reason for the empirical observation that morning and evening sunlight often appears more red-shifted, while mid-day sunlight has a more bluish and white appearance. SZA related red-shift is explained mostly by Rayleigh scattering which is inversely proportional to the fourth power of the wavelength [14].

Cloud cover can also have a significant effect on the terrestrial solar spectrum. Different cloud types have different absorption and scattering properties within the solar irradiance spectrum depending on the thickness, altitude and water droplet (or ice crystal) properties of the cloud [21]. In this thesis, the data gathered is only from cloudless measurement days to avoid the large uncertainties related to spectral simulations in cloudy weather. This data selection allows for increased calibration accuracy and closer match to the AM1.5D and AM1.5G spectra, which are specified for cloudless conditions [12] [20]. For these reasons, cloud effects are not further discussed in this thesis.

Though the sky might be cloud-free, there is always water vapour in the atmosphere. The water vapour content of the atmosphere is determined by complex relations in the climate and it changes through the seasons with large variations often also in the timescale of days and weeks [22]. The water vapour content of the atmosphere is characterized by Total Precipitable Water (TPW), which defined as the depth of the liquid water column if all the water vapour in the atmosphere was precipitated as rain [22]. The effect of atmospheric water vapour is then simplified to calculation of attenuation through this imaginary water column which follows the Beer-Lambert law [23]. Water has many absorption bands in the solar spectrum, with the greatest attenuation bands located in the infrared range [22], at some of which the irradiance often almost completely disappears. Therefore, the atmospheric water vapour has the most effect on the performance of those solar cells which are active in the infrared range. The most significant absorption bands of water on the solar irradiance spectrum are marked in Figure 2.4.

Other gases in the atmosphere have many absorption peaks in the solar irradiance spectrum. Ozone has strong scattering properties in the ultraviolet and short visible wavelengths. The strength of this effect is proportional to the thickness and concentration of the ozone layer in the stratosphere. [22] Oxygen and carbon dioxide also have absorption bands along the solar irradiance spectrum. The effects of these gases on the solar irradiance spectrum are marked in Figure 2.4.

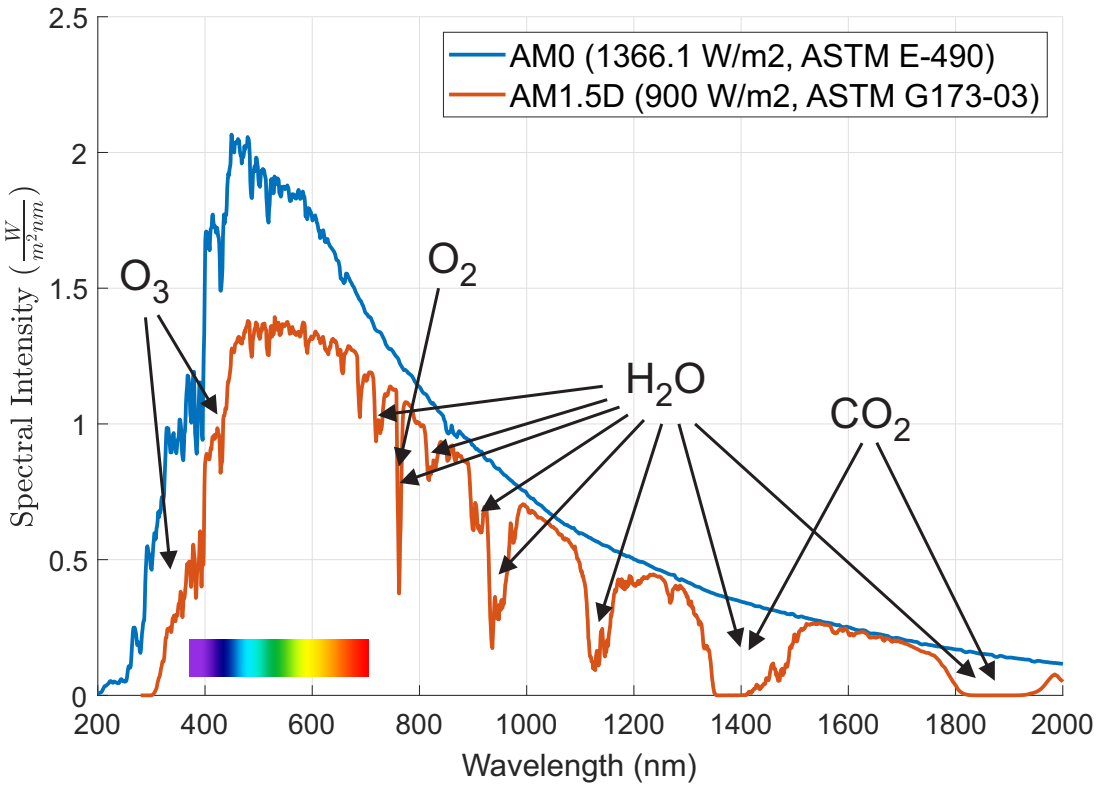

Figure 2.4. *Effect of the most significant absorption bands of atmospheric gases on the solar irradiance spectrum. Comparison between AM0 extraterrestrial spectrum and AM1.5D terrestrial spectrum. Gas absorption bands gathered from [22].*

Aerosols, which are suspended fine particles in the atmosphere, also have scattering and absorption effects along the whole solar irradiance spectrum [20]. The attenuation depends on the concentration and particle size distribution of aerosols in the atmosphere [24]. As extreme examples, smog can significantly attenuate the solar irradiance in large cities, with similar effect occasionally happening from volcano eruptions.

2.1.3 Simulation of spectral radiation

Simulation of solar irradiance is a cost-effective and widely scalable method to produce terrestrial spectral irradiance data. Such data can be used in analyzing and predicting photovoltaic energy production, for example [25]. The cost-effectiveness is achieved by removing the need for expensive spectrometers, pyranometers and pyrheliometers for sunlight characterization. The cost of such complete measurement system can easily climb into six figures, also requiring frequent calibration and maintenance to maintain their accuracy. Another benefit is that the spectral simulation can be performed for any location around the world due to wide availability of open-source atmospheric data. In contrast, spectral irradiance measurement systems are limited to few specific locations, and the data is not as freely available as atmospheric satellite data. Some of the atmospheric data used in this thesis is available for spans of decades, which can allow for long-term performance analysis and energy generation estimates of solar modules. This information can then be used in designing photovoltaic power plant locations and capacities. In this thesis, the simulated spectral data is used to calculate the calibration targets for the calibration method. [21]

Simulation of spectral radiation can be roughly divided into two methods. In statistical methods, solar spectra are calculated based on the cross-comparison of large amounts of satellite data and corresponding terrestrial spectrometer measurements. In physical methods, radiative transfer equations are used to solve for solar radiation transmission through the simulated atmosphere, which is often created on the basis of satellite data. In this thesis, the simulated spectral data is based on the physical radiative transfer method. [26]

2.1.4 Radiative transfer method

In the radiative transfer (RT) method, radiative transfer equations (RTE) are used to solve for the interaction of solar radiation with gases, liquids and aerosols in the atmosphere to create a simulated solar spectrum in the target location [25]. They all start with the extraterrestrial irradiance spectrum at the top of the atmosphere. The spectrum is then attenuated when the light travels through the atmosphere to reach ground level. RTE calculations have best accuracy in clear-sky conditions, while any cloud cover introduces large variations in the accuracy [26]. The uncertainty of simulated direct solar irradiance in clear-sky conditions is estimated to be about 3 % while in cloudy weather the uncertainty can be tens of percents. Especially in rapidly changing weather conditions,

where the cloud cover can significantly change in less than an hour, satellite data is too unreliable to produce accurate results by RT method [27].

Many different RT models exist with different physical and atmospheric assumptions and complexity. Most RT models are so-called clear sky models, in which the sky is assumed as completely cloudless. Their input data consists of the Sun position and atmospheric data of ozone content, aerosol optical depth, water vapour content, as well as other less significant parameters. The most widely used software for solving the RTE is the SMARTS model, while other models include e.g. SOLIS, ESRA and LibRadTran. In this thesis, the clear sky spectral simulations were performed with the libRadTran library for radiative transfer [28]. [26]

2.2 Solar simulators

Solar simulators are laboratory devices which mimic the radiation of the real Sun. They consist of a light source, collimation and guiding optics, and optical filters to closely match the solar standard spectra on a working surface. A well-calibrated solar simulator is a great platform for characterization of research solar cells, creating much more consistant and reproduceable results than those measured in outside conditions.

Solar simulators can be roughly divided into two categories based on their irradiance. One-sun simulators aim to reproduce the standard solar spectra discussed in Chapter 2.1.1. Concentrated photovoltaics (CPV) simulators can create concentrated sunlight with intensities up to thousands of suns [29].

2.2.1 Solar simulator standards

Solar simulators need to be well calibrated to match the reference spectrum in order to produce reliable measurement results. At the time of writing this thesis, the active standard for solar simulator performance is the ASTM E927-19 standard [11]. The irradiance characteristics of a solar simulator are ranked in three main categories: temporal instability, spatial non-uniformity, and spectral match. Each of these parameters are have performance classes A, B and C, with an additional class U (unclassified) for those simulators whose performance parameters rank outside of the ABC classes. [11] [29] The class requirements are presented in Table 2.1.

Table 2.1. *ASTM E927-19 standard classifications for solar simulators [11].*

Classification	Temporal instability T_{IE}	Spatial non-uniformity S_{NE}	Spectral match R_{SM}
A	$\leq 2\%$	$\leq 2\%$	$0.75 \leq R_{SM} \leq 1.25$
B	$\leq 5\%$	$\leq 5\%$	$0.60 \leq R_{SM} \leq 1.40$
C	$\leq 10\%$	$\leq 10\%$	$0.40 \leq R_{SM} \leq 2.00$
U	$> 10\%$	$> 10\%$	$R_{SM} > 2.00$

Temporal instability describes the variance in total irradiance over time at the illumination area of the solar simulator [11]. It is critical that the irradiance spectrum remains constant during and between measurement sets to allow for accurate and reproduceable results. Many factors can introduce temporal instability, for example thermal fluctuations in the light source and optics, noise in the driving electronics, or mechanical vibrations inside the simulator.

Spatial non-uniformity describes the variation of irradiance inside the illumination area. The goal is to form an uniform irradiance spectrum at every point along the surface area of the sample. Good uniformity over a large working area allows for more accurate and reproduceable results.

Spectral match describes the similarity between the illumination spectrum and the refer-

ence spectrum. It is specified in the wavelength range from 400 nm to 1100 nm for the AM1.5D and AM1.5G spectra, and in the range from 350 nm to 1400 nm for the AM0 spectrum. The spectral match is characterized separately for each 100nm wide wavelength band as the ratio of the simulator irradiance and the reference irradiance. The spectral match in each wavelength band is calculated and the total spectral match classification is defined as the lowest classification from all of the spectral match values. [11] The spectral match class limits are illustrated in Figure 2.5 for each wavelength sub-band for the AM1.5D standard spectrum. One can imagine all the possible spectra that would fit inside the classification limits, with quite high mismatch of up to 25% also allowed in the highest A class specification.

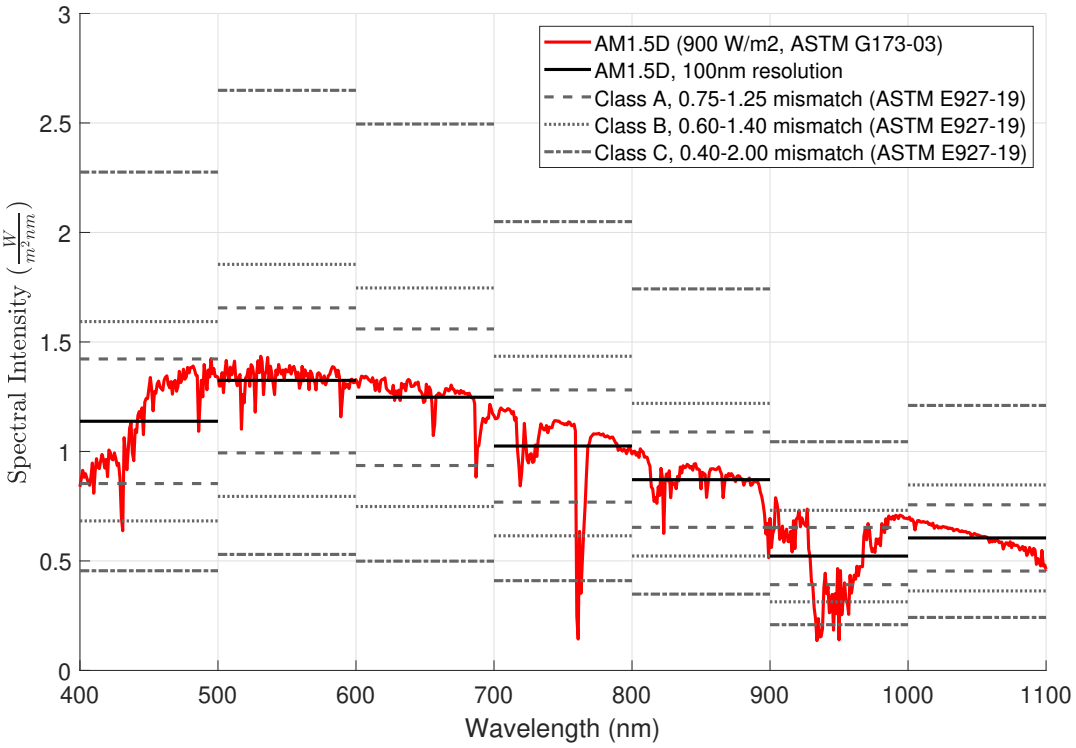

Figure 2.5. *Solar simulator spectral mismatch classes A, B, and C according to ASTM E927-19 [11]. Reference spectrum AM1.5D (ASTM G173-03 [12]).*

Solar simulator classification is presented as the combination of these three metrics. The best possible classification is AAA, while a less accurate simulator might have classification BCC for example. In such a case, it must be separately noted which letter corresponds to which classification metric. [11]

2.2.2 Solar simulator types

The most important factor in solar simulators is the light source. Traditionally the most common light sources for solar simulators are arc lamps, which produce light by electric arcs through gas between metal electrodes. Common gases inside the lamp are xenon,

carbon and argon, for example, with some variants also using metal halides as the arc medium [29]. During the 2000's, more advanced solar simulators have started to feature LED arrays and super continuum lasers as the light source, which can allow for increased accuracy, optical efficiency, and tunability [29]. In this Chapter, two existing simulators in the ORC laboratory are presented: the OAI Trisol CPV Solar Simulator and the G2V Optics Pico Solar Simulator.

The OAI Trisol is a class-AAA solar simulator which features a 7 kW xenon-arc lamp as the light source [30]. It has two operation modes: large-area one-sun illumination and small-area CPV illumination of up to 1500 suns through modular concentrator optics. The Trisol has been used extensively in solar cell research at ORC since 2016. While the Trisol has been useful in research, it does have a few disadvantages that have lead to increasing problems when measuring MJSC photovoltaics with four or more junctions. The xenon arc lamp has very limited spectral tunability and the aging of the lamp changes its spectrum significantly, which leads to large deviations in the MJSC measurements. Though the simulator is originally ranked in the AAA-class, its spectral accuracy, tunability, and temporal stability has been shown by extensive testing to be less than optimal for modern MJSC research. The main benefit is the very high irradiance of up to 1500 suns, which is crucial for concentrated photovoltaics research. The Trisol simulator is a very large instrument that requires powerful cooling, as can be seen in Figure 2.6.

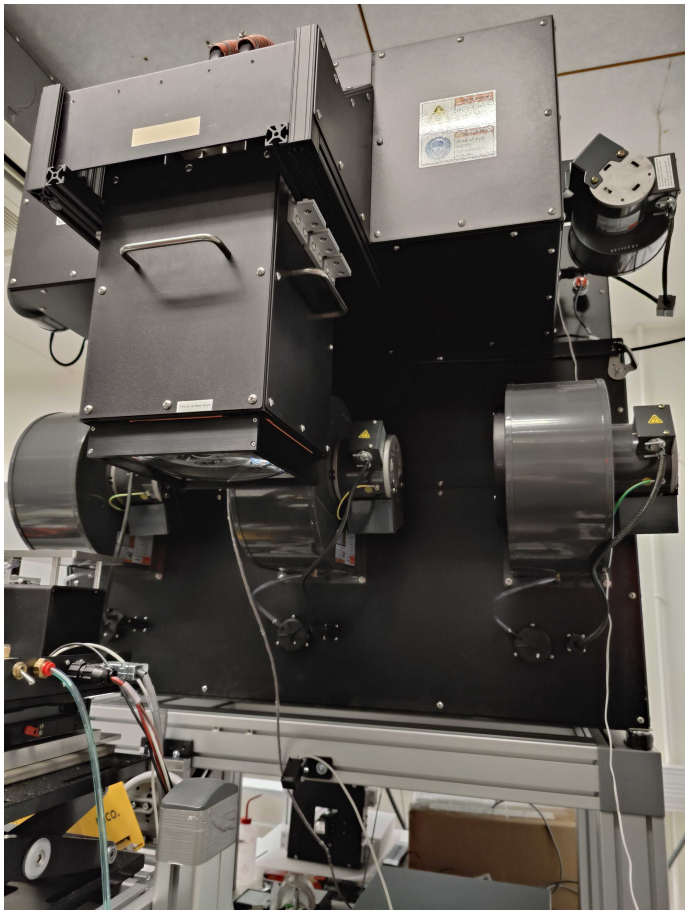

Figure 2.6. *The OAI Trisol solar simulator.*

The G2V Pico AAA-class LED solar simulator [31] was deployed in 2022 at ORC to improve on some of the disadvantages mentioned for the Trisol simulator. Its LED array has 32 fully adjustable wavelength channels in the range 350-1500 nm. The spectral match for the Pico far exceeds the ASTM E927 A-class requirements, with less than 5% mismatch possible as specified by the manufacturer. The included software allows for full control of the LED array to replicate essentially any terrestrial spectrum, and most importantly the ASTM standard spectra. The wide tunability is extremely useful in research of MJSC samples at ORC which are very sensitive to spectral variations. Due to its use of LEDs, the Pico's temporal stability is significantly better than for the Trisol.

The drawbacks of the Pico include the maximum irradiance of one-sun illumination and that the working area is only 25 mm x 25 mm, which can be a limitation for larger samples. The Pico is a very compact tabletop instrument compared to the Trisol. Overall, based on its specifications, the Pico can be considered as a well suitable device for first application of the thesis calibration method. The device and its LED array are visible in Figures 2.7 and 2.8.

Figure 2.7. *The illumination head of the G2V Pico solar simulator.*

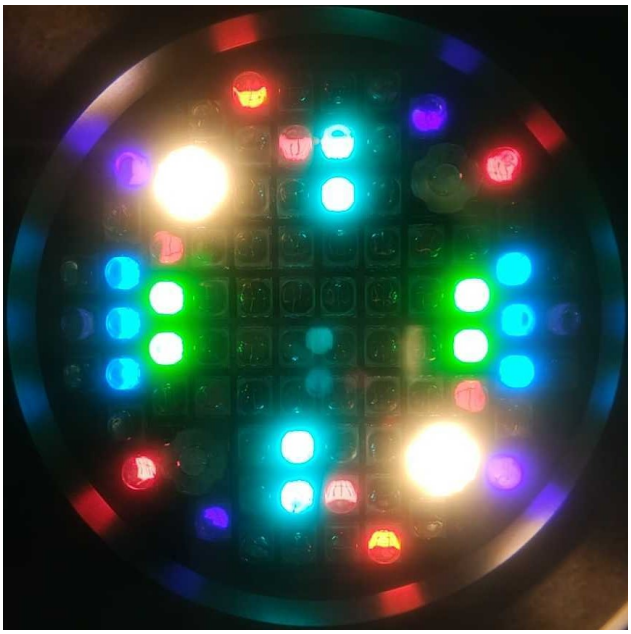

Figure 2.8. *The LED array of the G2V Pico solar simulator. The LEDs near the center of the array are operating in infrared wavelength ranges, thus being invisible to the human eye.*

2.3 Basics of semiconductor solar cells

Semiconductor solar cells are devices that absorb solar radiation and convert it to electrical power. They are made from different semiconductor materials, most commonly silicon or gallium arsenide, while more recent advanced designs include a wide range of other semiconductors. [5] In this Section, the basic operation of semiconductor solar cells is discussed, continuing with a brief overview of the basics of multi-junction solar cells.

2.3.1 The p-n junction

Semiconductor solar cells are based on the p-n junction. The p-n junction consists of p-type and n-type semiconductor materials which form a connection at the interface. The electrical properties of the semiconductor layers can be adjusted by doping, a method in which other elements, so called "dopants", are introduced into the semiconductor lattice in the growth phase which results in excess charge carriers being released into the conduction band. In a p-type semiconductor, these positively charged excess carriers are called holes, while in an n-type semiconductor the carriers are negatively charged electrons. Figure 2.9 shows the structure of a p-n junction. [17] [32]

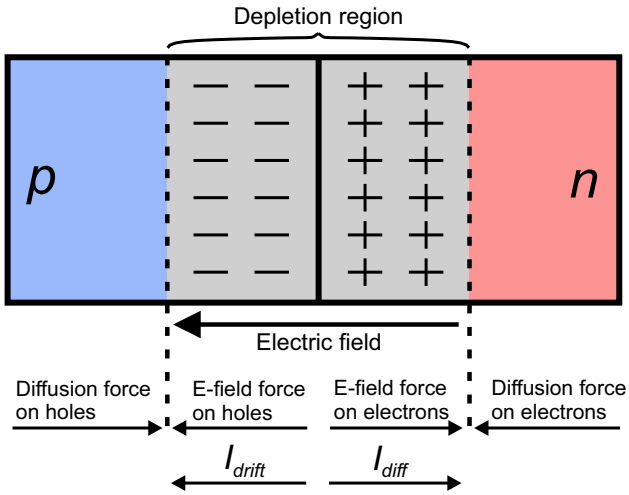

Figure 2.9. *Simple illustration of the semiconductor p-n junction.*

When the p-type and n-type semiconductors are fused together e.g. by epitaxial growth, the conduction band electrons in the n-region start to diffuse towards the p-region and the valence band holes from the p-region diffuse towards the n-region [32]. The holes and electrons recombine when they meet at the interface, creating a region which has no free charge carriers in the conduction band, which is called the *depletion region*. The dopant ions in the semiconductor lattice can not act as charge carriers, however they do cause an electrical charge in the depletion region which is negative in the p-region side and positive in the n-region side. This electrical charge distribution creates an electric field in the depletion region which points towards the p-region. [32] [33]

When electrical contacts are connected to the opposite ends of the p-n junction, the device's electrical characteristic follows the diode equation in dark conditions [33]

$$I_{dark} = I_0(e^{\frac{qV}{nkT}} - 1), \tag{2.2}$$

where q is the elementary charge, V is the applied voltage, n is the ideality factor of the diode, k is the Boltzmann constant, T is the temperature and I_0 is the dark saturation current, also called the diode leakage current.

P-n junction solar cells are designed so that photons are absorbed in the depletion region or within diffusion length's distance from it. This provides a basis for the *photovoltaic effect*, in which a voltage and current can be generated from the incident light if the photon has sufficient energy. [32] Incident photon energy E_{phot} is calculated by

$$E_{phot} = hf = \frac{hc}{\lambda}, \tag{2.3}$$

where h is the Planck's constant, f is photon frequency, and λ is photon wavelength. If the photon energy is greater than the bandgap energy of the semiconductor, $E_{phot} > E_g$, the photon can generate an electron-hole pair inside the semiconductor. If the photogenerated minority charge carrier is approximately within diffusion length's distance from the p-n depletion region, the charge carrier can diffuse into the depletion region. The electric field then directs a force on the charge carrier, making it drift over to the opposite region of the p-n junction. This drift across the depletion region is called *charge collection*. Under continuous illumination, the light-generated drift current is called the *photocurrent*, and the related electrical charge build-up across the p-n junction is called the *photovoltage*. Ideally, the photocurrent is independent of the voltage across the operation range of the solar cell. [17]

The photocurrent and dark diode current are combined to reach an ideal equation form for the electrical characteristic of the solar cell

$$I = I_{dark} + I_{phot} = I_0(e^{\frac{qV}{nkT}-1}) + I_{phot}. \tag{2.4}$$

This form of the current-voltage (IV) curve is the most simple and ideal version and an example is illustrated in Figure 2.10. In reality, many different phenomena such as electron-hole recombination and, series resistance and shunt currents can significantly affect the IV characteristic of real solar cells further from this simplified example. [33] [17]

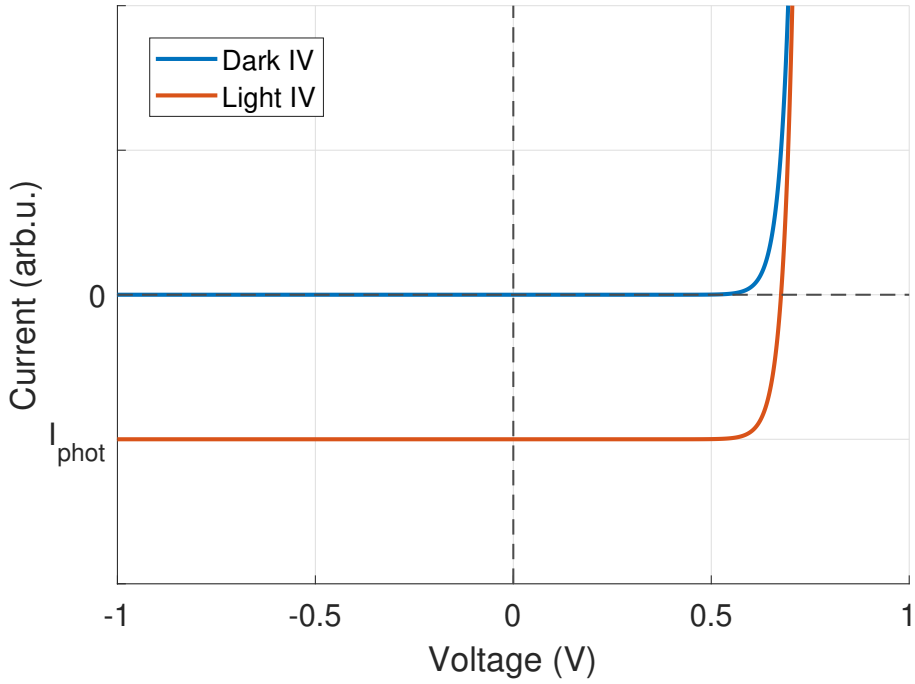

Figure 2.10. *Example of a p-n junction solar cell IV curve in dark and light conditions.*

A solar cell operates in the fourth quadrant of the light IV curve of Figure 2.10, providing electrical power to be utilized in an external circuit. Characteristics of the IV curve are further discussed in Section 2.3.3.

2.3.2 Simple structure of a semiconductor solar cell

Semiconductor solar cells are based on the p-n junction and its electrical characteristic [33]. Example structure of a simple p-n junction solar cell is illustrated in Figure 2.11.

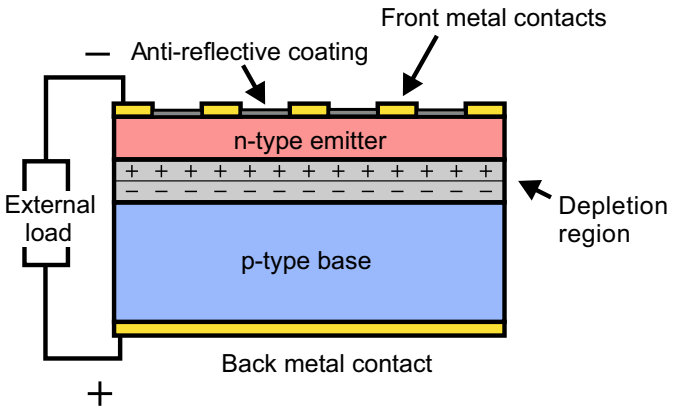

Figure 2.11. *Basic structure of a semiconductor solar cell based on the p-n junction.*

This simple solar cell is built around the p-n junction, with metal contacts fabricated on top and bottom surfaces which are connected to an external load [34]. Incident photons

with sufficient energy are absorbed in the semiconductor layers, generating electron-hole pairs. Ideally this electron-hole generation happens inside the depletion region or within diffusion lengths distance from it, which allows for charge collection by the p-n junction as discussed in Section 2.3.1. The solar cell operates inside the fourth quadrant of the light IV curve in Figure 2.10, providing electrical power to the external load. The top metal contact grid design is a critical aspect of creating a highly efficient solar cell: the task is to collect charge carriers efficiently to the external circuit while also minimizing the grid area to avoid shadowing the solar cell surface. An anti-reflective coating is fabricated on the top surface of the solar cell to maximize photon transmission into the semiconductor material which increases the photocurrent. [34]

2.3.3 Parameters of the current-voltage curve

In this Section, the most important parameters of the solar cell current-voltage characteristic are presented. These parameters can be extracted from the IV curve of Figure 2.10. For convenience, the IV curve current axis is often inverted in solar cell IV characteristics to get positive values for both current and voltage in the operation quadrant. The IV curve is often measured in a four-point probe setup to avoid voltage losses in the measurement circuit, providing increased accuracy. The characteristics are measured and reported under illumination of the ASTM solar spectra. Figure 2.12 shows the most important parameters in the light IV curve of a solar cell.

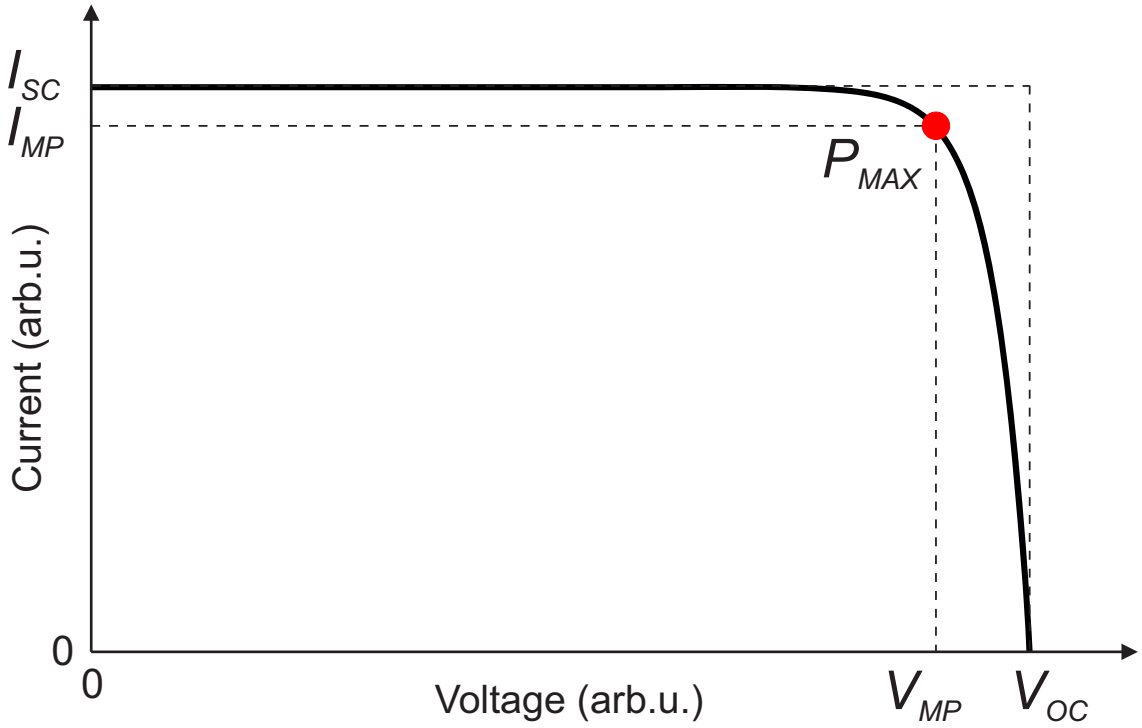

Figure 2.12. *Example light IV curve of a solar cell with most important parameters highlighted. Current axis inverted for convenience.*

The short-circuit current I_{sc} is an important parameter to evaluate the photocurrent generation performance of a solar cell. It is defined as the current that is generated under illumination when the voltage across the sample is zero, i.e. the contacts are short circuited. I_{sc} is strongly dependent many different factors such as material choice, absorption, charge collection, recombination and grid shadowing. [17]

For easier comparison between samples with different surface areas, the current generation characteristics of a solar cell is often reported in terms of the short-circuit current density J_{sc} which is defined as the ratio of short-circuit current and the surface area A of the solar cell

$$J_{sc} = \frac{I_{sc}}{A}. \tag{2.5}$$

The open-circuit voltage V_{oc} is used to evaluate the voltage generation performance of a solar cell. It is defined as the voltage that is generated under illumination when there is no load connected to the contacts. V_{oc} for a given incident irradiance is strongly dependent on the material band gap and quality. [17]

At the "knee" of the IV curve is the maximum power point (MPP). Solar cells are ideally operated in close proximity to the MPP by choosing and adjusting the external load [34]. The MPP is defined as the point where the generated electrical power is maximized, i.e. the product of current and voltage is highest

$$P_{max} = I_{mp}V_{mp}. \tag{2.6}$$

Another important parameter of solar cell quality is the *fill factor* (FF). Its value for a solar cell can theoretically range from 0% to 100%, and is defined by

$$FF = \frac{P_{max}}{I_{sc}V_{oc}}. \tag{2.7}$$

An intuitive way of visualizing the fill factor from the IV curve is to evaluate the "squareness" of the IV curve. It is the ratio of the two rectangular areas in Figure 2.12. High quality solar cells can have fill factor values nearing 90%, which allows towards achieving very high conversion efficiencies. The fill factor can be reduced by many effects such as material defects, resistive losses and shunt ("leakage") current. It is also dependent on the material band gap. [17]

Arguably the most important solar cell parameter is the power conversion efficiency η, which summarizes the photovoltaic performance into a single value. It is defined as the ratio of maximum generated electrical power P_{max} to the incident optical power on the solar cell surface P_{in}. Using Equation 2.7, it can be written as

$$\eta = \frac{P_{max}}{P_{in}} = \frac{FF \cdot I_{sc}V_{oc}}{P_{in}} \tag{2.8}$$

For maximizing the efficiency of a solar cell, a good combination of high fill factor, short-circuit current and open-circuit voltage is required as can be seen in Equation 2.8. Optimizing the efficiency is a complex process which involves many optimizations in the material quality, layer thicknesses, contact grid design, antireflection coatings and thermal management among other factors. [34]

2.3.4 Quantum efficiency

The quantum efficiency of a solar cell is a widely used metric for determining the sample's conversion efficiency of photons into charge carriers. Quantum efficiency is wavelength-dependent and strongly affected by semiconductor material choice and quality, absorption efficiency and recombination rate among many other factors. Two important quantum efficiency characteristics exist for solar cells: the external quantum efficiency (EQE), which describes the current generation ability of the whole sample, and the internal quantum efficiency (IQE) which describes the charge collection properties of the semiconductor material. For the purposes of this thesis, EQE is the more useful metric. [17]

EQE is often measured under short-circuit conditions, and it is defined as the ratio between the number of collected charge carriers and the number of incident photons on the solar cell surface

$$EQE(\lambda) = \frac{\text{\# collected charge carriers}}{\text{\# incident photons}} = \frac{\frac{1}{q}I_{sc}}{A\Phi_{in}(\lambda)} = \frac{\frac{1}{q}J_{sc}}{\Phi_{in}(\lambda)}, \tag{2.9}$$

where q is the elementary charge and $\Phi_{in}(\lambda)$ is the incident photon flux (units $\frac{1}{m^2 s}$). [17]

The EQE characteristic of a solar cell is measured using a tunable source of monochromatic light. The measurement setup is often based on a broadband lamp whose light is guided through a monochromator, which is a device that employs a diffractive grating to separate and select narrow sub-bands from incident broadband illumination. The EQE curve consists of a sweep of measurements over the whole active wavelength range of the sample. [17]

The EQE is related to the photocurrent of the solar cell. By rearranging Equation 2.9 and integrating over the whole active wavelength band of the sample, a useful expression for the short-circuit current density can be written as

$$J_{sc} = q \int_{\lambda_{min}}^{\lambda_{max}} EQE(\lambda) \cdot \Phi_{in}(\lambda) \cdot d\lambda, \tag{2.10}$$

where $\Phi_{in}(\lambda)$ is the photon flux of any spectrum under which the photocurrent is evaluated. The current density calculated by Equation 2.10 is often reported alongside the EQE measurement curve. However, many factors can introduce a mismatch between the real measured current density under illumination and the value approximated from EQE using Equation 2.10. A major assumption made in this approximation is that the EQE

is independent of photon flux, which is very different in the small-signal monochromatic EQE measurement compared to the full broadband illumination in the IV measurement. EQE is also often measured from a small spot in the sample surface, and in the calculation the EQE is approximated to be uniform over the whole sample area, which is not always accurate. Other factors that can introduce errors in the values obtained from Equation 2.10 include shunt currents and luminescence coupling among other phenomena. In spite of these potential error sources, the integrated photocurrent is often used as an easy comparison metric of EQE curves between different samples.

2.4 III-V multijunction solar cells

III-V multijunction solar cells (MJSC's) are solar cells which consist of multiple cell junctions, called sub-cells. The materials used for the subcells are semiconductors from the groups III and V of the periodic table. Different secondary, ternary, and quaternary combinations of these materials allow for creating subcells whose band gap and lattice constant can be adjusted by optimizing the material composition. [35] An example MJSC design is presented in Figure 2.13

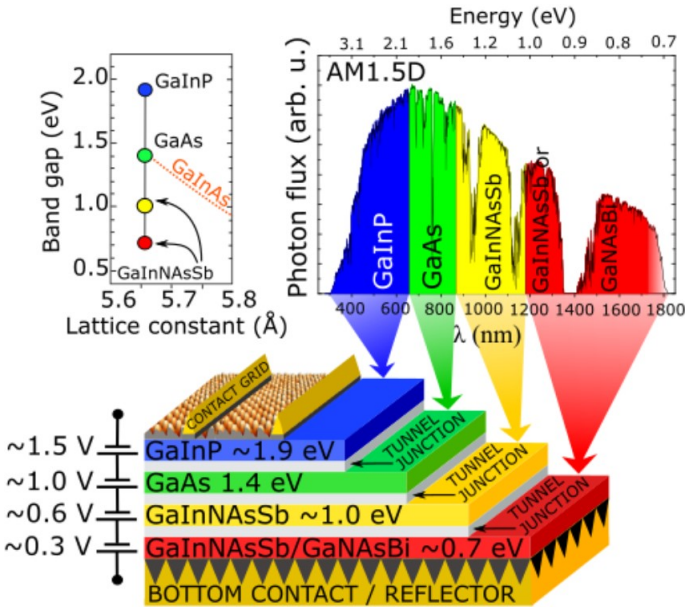

Figure 2.13. *Example design of a MJSC, showing the distribution of solar irradiance spectrum between the different subcells. Figure used with permission from Optoelectronics Research Centre. [36]*

In Figure 2.13, the MJSC subcells are electrically connected in series by tunnel junctions. Tunnel junctions are highly doped thin semiconductor layers which have near-zero resistance to avoid electrical losses and very low absorption which allows for efficient transmission of sunlight to the subcells below [35]. The subcells are arranged in order of descending energy band gap, with the highest energy (shortest wavelength) photons being absorbed in the first layer while the lower energy (longer wavelength) photons are transmitted through towards the next subcells to be absorbed there.

Because of the series connection between the subcells, the MJSC current is limited to the smallest photocurrent I_i in the stack

$$I = min(I_i). \tag{2.11}$$

Any excess current generated in the other subcells cannot be collected to the external circuit and the energy is lost. In order to reach the highest possible conversion efficiency, MJSC's are designed so that the subcells are *current-matched* under the application

spectrum. In practice, current-matching is optimized by adjusting the subcell layer thicknesses and band gaps which directly affects the absorption properties of the subcells. [35]

The series connection between subcells results in the subcell voltages V_i to be added together to form the total voltage of the MJSC

$$V = \sum V_i. \tag{2.12}$$

The additive voltage is the reason why MJSC's have high voltages compared to single-junction devices. For comparison, the highest efficiency single-junction silicon solar cell has an open circuit voltage of $0.74\,V$ [6], while the highest efficiency six-junction MJSC has an open circuit voltage of $5.55\,V$ [37]. Both of these results were measured under the AM1.5G standard spectrum [12].

For a single-junction solar cell, the choice of the material will affect the maximum voltage and current of the device. The operating voltage of a solar cell scales proportionally the band gap of the material, and the current scales inversely to the band gap [17]. While it may seem attractive to employ a small band gap device with e.g. band gap at 1600 nm to collect as many photons as possible from the solar spectrum, the voltage for such a device will be very small, resulting in low efficiency. Though most of the solar spectrum could be collected, only the band gap's worth of energy can be extracted each photon. This phenomenon is called *thermalization* which will lead to large losses at wavelengths further away from the band gap. Physically the high energy photon excites the electron to an energy state far beyond the conduction band edge, after which the electron thermalizes, i.e. releases its extra energy as heat when it quickly relaxes to the band edge. [17]

The high efficiency of MJSC's is largely due to more efficient power extraction from different parts of the spectrum. By employing many subcells with descending band gaps in the structure, the thermalization and transmission losses are significantly reduced when compared to single-junction cells. This way, a wide wavelength band from the solar irradiance spectrum can be extracted efficiently to provide high electrical power to the external circuit. The effect of the number of subcells to the thermalization losses is illustrated in Figure 2.14.

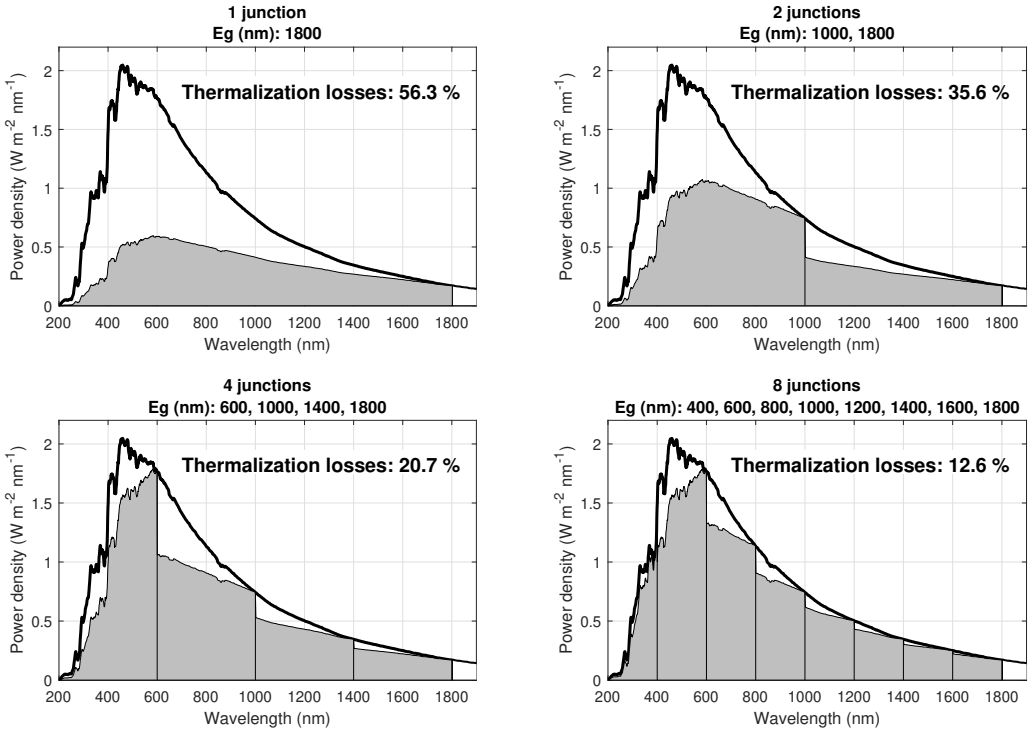

Figure 2.14. *The effect of the number of MJSC subcells on the thermalization losses. The reference solar spectrum is AM0 (1366 W/m2, ASTM E-490).*

In Figure 2.14, the subcells are assumed to collect all the photons shorter than their band gap (100% quantum efficiency), while no photons are absorbed at longer wavelengths than the band gap. Other loss mechanisms are neglected to emphasize the thermalization effects. The bottom cell band gap is fixed at 1800 nm, and the amount of subcells is varied between figures. The theoretical extracted power can be integrated from the gray area. The white area between the reference AM0 irradiance spectrum and the gray area corresponds to the losses, at wavelengths below 1800 nm are the thermalization losses and at wavelengths above 1800 nm are the transmission losses. The thermalization losses are clearly reduced when increasing the number of subcells. The transmission losses in this ideal approximation remain constant at about 8 %.

The same approximations are used in Figure 2.15, where the calculation of thermalization losses is extended for up to 20 subcells.

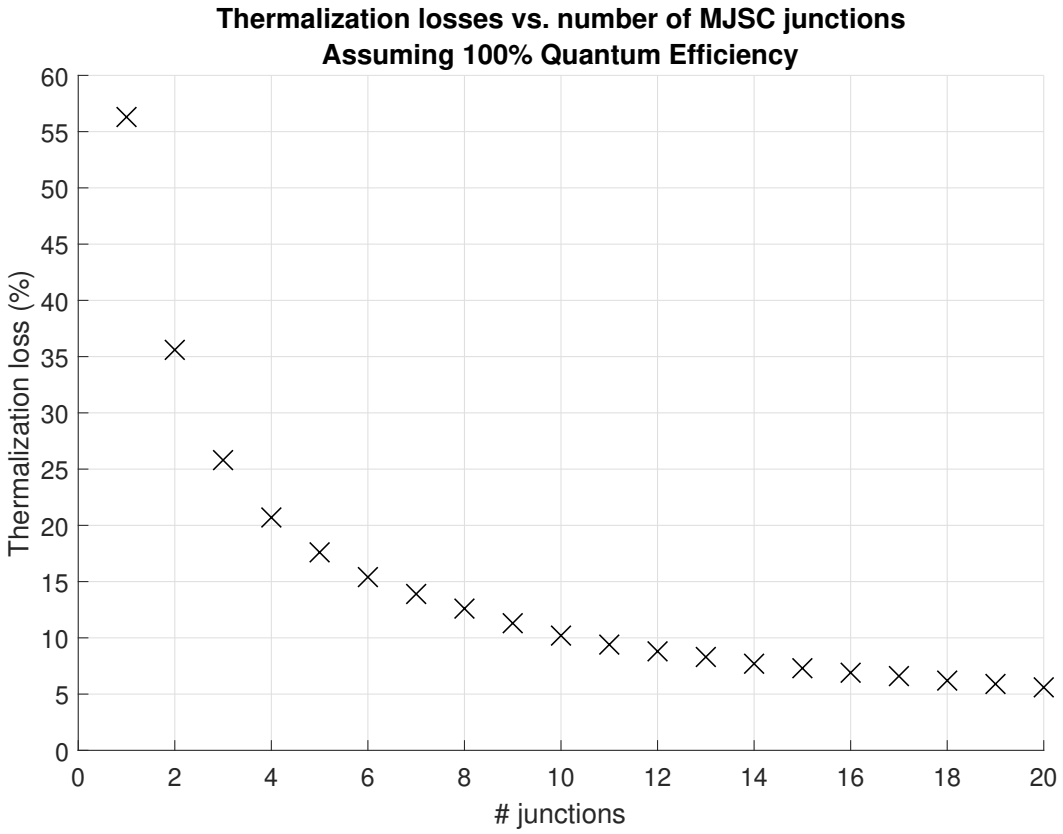

Figure 2.15. *Thermalization losses as a function of the number of MJSC subcells between 300-1800 nm for the AM0 spectrum. Ideal approximation assuming 100% EQE for each subcell.*

Figure 2.15 shows that there are diminishing returns in the loss reduction when increasing the number of subcells. The theoretical maximum efficiency under concentrated sunlight for a MJSC with infinite subcells is calculated by the detailed balance method to be 86.8% [38], but in reality such an efficiency is far out of reach due to limited availability of semiconductor materials and the non-ideal effects related to them as well as practical limitations in the fabrication process [8].

It is increasingly difficult to fabricate good quality semiconductors that are suitable for creating MJSC's with a high number of subcells. This introduces a practical limit for the number of subcells. Most commercial MJSC's have 3 or 4 junctions, while the most advanced research MJSC's have up to 6 junctions. The solar cell efficiency record as of writing this thesis is 47.6%, which was published by the Fraunhofer Institute for Solar Energy Systems in 2022. The device was a four-junction III-V MJSC and it was measured under irradiance corresponding to 665 suns. [7] For comparison, the record efficiency for a single-junction solar cell under concentrated sunlight is 30.8%. This result was measured from a gallium arsenide solar cell under 62 suns concentration, published by the National Renewable Energy Laboratory (2022). [39]

A common characteristic in III-V MJSC's is that their efficiency is greatly increased under concentrated sunlight in comparison to one-sun illumination. They are often illuminated

with an irradiance of hundreds or up to over a thousand suns. This technology is called *concentrated photovoltaics* (CPV), in which optical elements are employed to gather light from a large area to be concentrated to the relatively small cell [35]. Commonly used optics for CPV systems are spherical lenses, Fresnel lenses and parabolic mirrors. Such systems are built on top of a two-axis solar tracker that adjusts the orientation so that the optics and solar cell are always perpendicular to the Sun, maximizing the total generated energy. A major benefit of CPV technology is that it allows for high power generation from a small solar cell, which significantly reduces material costs and thus also lowers the cost per watt. [8]

MJSC's are an emerging technology in the field of photovoltaics (PV). Their total fabrication cost per watt is often beyond an order of magnitude higher than that of conventional silicon solar cells and thin film solar cells [8]. This is the main reason why the total terrestrial PV capacity of 848 GWp is dominated by silicon and thin film solar modules [5]. III-V MJSC's are currently mostly employed in applications where the goal is to generate maximal power in a limited surface area. Such applications include satellites, probes and stations in space, as well as drones and other small devices. Another benefit of MJSC's is their good endurance of exposure to gamma, proton and electron irradiation and atomic oxygen, which allows for a longer lifetime and much higher end-of-life efficiency in space applications compared to other PV technologies [8]. MJSC fabrication processes are constantly being optimized in pursuit of lowering the cost per watt to advance the installation rate of terrestrial CPV power plants.

2.4.1 Spectral sensitivity of multijunction solar cells

Multi-junction solar cells (MJSC) are designed to reach their maximum efficiency under the application spectrum. This involves intricate current-matching of the subcells as discussed in Section 2.4. If the incident spectrum differs from the design target spectrum, an imbalance will appear in the subcell currents. The current imbalance introduces losses which can significantly decrease the overall efficiency of the MJSC [35].

As an example, we can consider the MJSC structure in Figure 2.13. If the UV- and visible wavelength band photon flux between 300-650 nm is attenuated by 20% in comparison to the target spectrum, the MJSC current is decreased by 20%, assuming the top subcell acts as the current limiter. For a single-junction device in the same situation, e.g. silicon solar cell with active wavelength range from 300 to about 1100 nm [40], the loss in current would be a small fraction in comparison because the total photon flux attenuation in its active range would be much less than 20%. In other words, the MJSC is much more sensitive to irradiance changes in small sub-bands of the spectrum when compared to 1J devices. Extra losses in an MJSC can be introduced also because the subcells will operate away from their optimized maximum power point due to the change in current, leading to a relative decrease of more than 20% in the efficiency. In spite of such a large error, the solar simulator in this measurement could still be classified in the highest A

class according to the ASTM E927 [11] standard, which allows for up to 25% spectral mismatch as discussed in Section 2.2.1.

Because of the current balancing and related spectral sensitivity, MJSC research requires well-calibrated illumination sources to produce reliable and reproduceable results for valid comparisons within the scientific community. With increasing number of junctions, the MJSC becomes more and more sensitive to spectral variations and inaccuracies. The highest solar simulator standard, class A, allows for up to $\pm$ 25% irradiance mismatch in each 100nm sub-band of the spectrum, as is presented in Section 2.2.1. Considering the discussion above, this specification can be a large error source in MJSC measurements. The main goal of this thesis is to create a calibration method which can be used to calibrate a solar simulator beyond the A class spectral match to allow for improved accuracy in MJSC research results.

3 EXPERIMENTAL

The experimental work of this thesis is presented in this Chapter. In Section 3.1, the calibration method is presented. The calculated calibration data is then used in calibration of two different solar simulators in Section 3.2. In Section 3.3, the effect of spectral mismatch on the multi-junction samples is investigated. The accuracy and reliability of the research results are further discussed in Section 3.4.

3.1 Calibration by outside measurements

The goal of this thesis is to calibrate a solar simulator using measurement data from outside measurements under real sunlight. Spectral match with better precision than the A classification (ASTM E927-19 [11]) was selected as the target. The calibration data is measured under real-sun illumination in an outside measurement setup. Each outside measurement set is analyzed with the corresponding simulated spectrum to calculate the expected current density of the samples under ASTM standard spectrum illumination. This current density value is then used as a target in the calibration of the solar simulator which is performed by using the same samples.

The main benefits of this method include high accuracy, spectral width and cost-effectiveness. The high accuracy is achieved by using a large dataset of outside measurements with many samples that have different spectral responses. The large spectral width of the calibration is achieved with careful selection of samples with different EQE responses in the wavelength range from 300 nm to 1600 nm. The setup itself costs no more than a few hundred euros, while calibration at a verified calibration facility often costs multiple thousands of euros per sample. The added cost of including additional samples to this setup is negligible.

3.1.1 Outside measurements: samples, setup and procedure

The outside measurement samples were selected from III-V solar cells fabricated at the Optoelectronics Research Centre (ORC) of Tampere University. Sample selection was based on their active wavelength range to allow for calibration in those wavelength bands which are most needed in research at ORC. Calibration is performed using single-junction (1J) samples, whose combined active range spans roughly from 300 nm to 1600 nm. The External Quantum Efficiency (EQE) curves of the six calibration samples are presented

in Figure 3.1. The samples are named in running numbers, with their approximate band edge in nanometers indicated inside brackets.

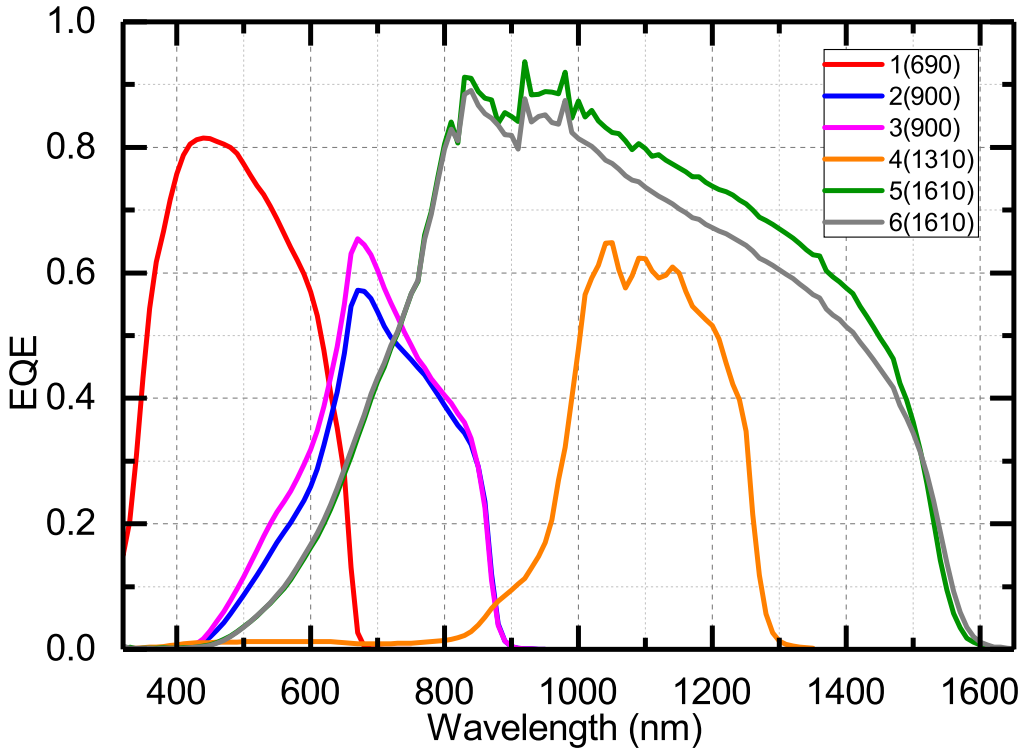

Figure 3.1. *The external quantum efficiency (EQE) curves of the 1J calibration samples.*

The basic unit of the outside measurement setup is the sample mount for the solar cell. The cell contacts are terminated to a cable with a four-point setup to allow for accurate current-voltage measurements. The back of the sample is thermally connected to a large aluminum plate. A Fused silica (FS) window is installed on top to avoid dust or other contaminants accumulating on the sample surface. A lens tube is added on top with an adjustable iris to adjust the angular aperture of incident sunlight to the sample. On the side of the lens tube is a 3D printed dual pinhole system to assist in the alignment towards the sun. Figure 3.2 includes a cross-section illustration and a picture of the sample mount.

The sample mounts are installed on an aluminum plate. The plate stand includes two rotation stages perpendicular to each other to allow for adjusting the system orientation precisely towards the sun. The plate temperature is monitored with a thermocouple. The sample mounts are covered with reflective aluminum tape to minimize the heating of the system under sunlight. The setup is pictured in Figure 3.3.

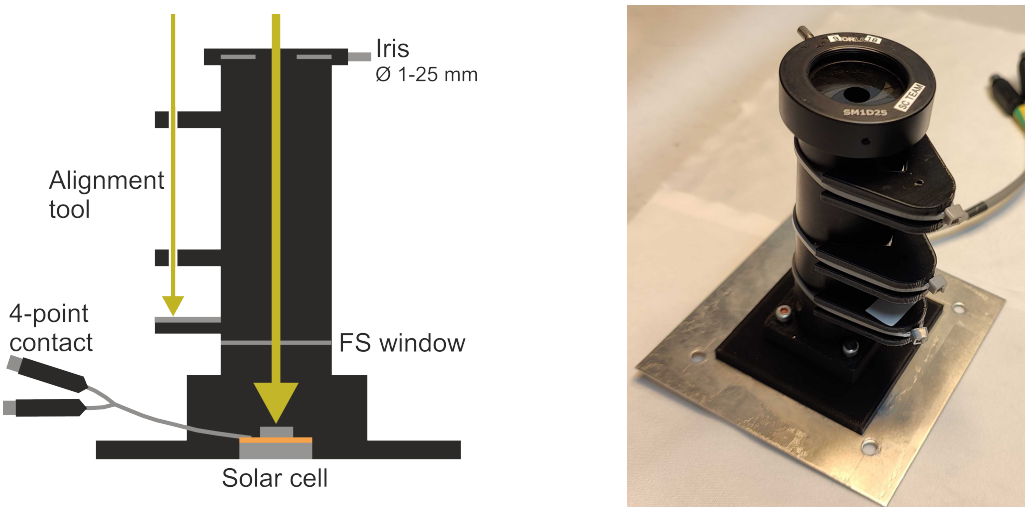

Figure 3.2. *Cross-section illustration (a) and picture (b) of the solar cell sample mount*

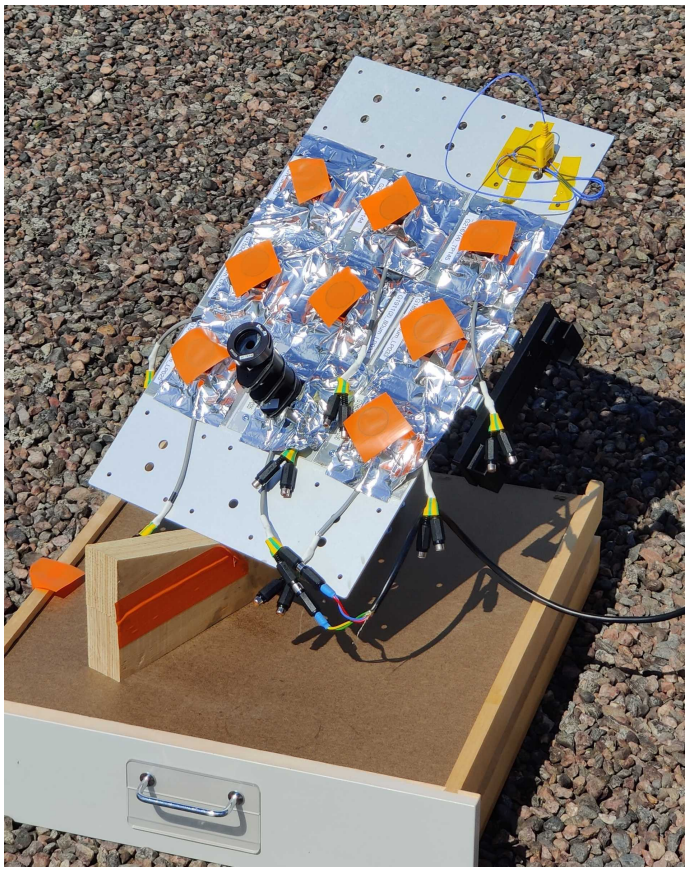

Figure 3.3. *The outside measurement setup with 9 samples mounted.*

Coarse alignment of the setup was performed using the pinhole alignment tool. Fine tuning of the orientation was performed before each measurement by making slight angular adjustments until the photocurrent of the sample was maximized, which corresponds to perpendicular alignment to the sun.

The current-voltage measurements were performed using a Keithley 2450 sourcemeter in four-point measurement mode. The voltage sweep resolution was set to 5 mV. Each sample was measured three times in succession with full aperture angle of 5.8°, 10° and 25° by adjusting the iris diameter and lens tube length. The 5.8° circumsolar angle corresponds to the direct solar radiation as specified in the AM1.5D standard [12], while the other two angles can be used to characterize the angular distribution of diffuse irradiance.

The measurement dataset consists of 13 measurement instances during June, July and August of 2022. The measurement instances had varying cloud cover and solar zenith angles. The data analysis was restricted to six of these instances where the cloud was completely cloud-free, producing the most reliable results and following the clear-sky approximation made in the spectrum simulation. In addition, some of the measurements had to be discarded due to other technical difficulties in the setup. The measurements were performed during mid-day hours when the sun was near zenith which often produces the best match to AM1.5 standard spectra in the latitude of Tampere, Finland.

3.1.2 The simulated solar spectra for outside sessions

In this thesis, the simulated spectra were provided by the Finnish Meteorological Institute (FMI) and they were solved using the libRadTran model. LibRadTran is a free library for radiative transfer consisting of a collection of C and Fortran functions and programs. It was first introduced in 2005 [41] and has since been further developed in many iterations, with the latest update in 2020. LibRadTran has been used in over 400 scientific publications. [28]

The simulations were performed in the latest libRadTran version 2.0.4. The radiative transfer equations were solved using *rte_solver twostr* two-stream method with the pseudospherical add-on, which accounts for the real curvature of the Earth. The simulation builds on an atmospheric standard profile for mid-latitude summer created by the US Air Force Geophysics Laboratory [42], which can be considered a good choice to simulate the atmosphere also in Finland.

Atmospheric gas absorption was calculated by *reptran coarse* option which is a parametrized method for approximating spectral absorption in the atmosphere. Atmospheric aerosol effects were based on the *default aerosol* option of LibRadTran, which was slightly tweaked to match typicals values of aerosol optical depth (AOD), single-scattering albedo (SSA) and aerosol asymmetry parameter (AAP) in Finland. The atmospheric aerosol properties were not from daily measurements, however their effect on the solar irradiance can be considered as relatively constant during the summer under normal conditions. There were no noticeable differences in the aerosol content between the measurement sessions: the sky was always fully clear and no haziness or smog was detected.

The Total Precipitable Water (TPW) values for the measurement sessions were obtained as hourly data from ERA5 database which is maintained by The European Centre for Medium-Range Weather Forecasts (ECMWF). ERA5 has been iterated and optimized by

a long history of reanalysis of atmospheric measurements. It provides hourly data on a vast range of atmospheric parameters since 1959 [43].

The total ozone column (TOC) was obtained from the OMI dataset which is measured by the Aura satellite maintained by the National Aeronautics and Space Administration (NASA) [44]. It provides daily overflight data on the TOC also over Tampere, Finland.

Surface spectral albedo was obtained from the built-in libRadTran library of the International Geosphere-Biosphere Programme (IGBP) [28]. Surface spectral albedo describes the spectral reflectivity of the Earth's surface, which then affects the diffuse irradiance. [22]

The simulations were performed assuming clear-sky conditions, which is an accurate approximation because the solar cell measurements were performed in cloudless conditions. This way, a close spectral match could be achieved to the AM1.5D spectrum, which is the main calibration target of this thesis. The solar spectrum was simulated with a five minute resolution over all of the measurement sessions.

The measurement instances are listed in Table 3.1 which also lists the corresponding simulated solar irradiances. The simulated solar spectra are listed as Figures in Appendix A.

Table 3.1. *Outside measurement sessions selected for calibration analysis. Table includes the simulated direct and diffuse solar irradiances for the sessions. Simulated irradiance spectra for the sessions are plotted in Appendix A.*

Session #	Date yyyy-mm-dd	Time UTC	SZA °	Direct irradiance W/m^2	Diffuse irradiance W/m^2	Figure #
1	2022-06-06	09:30 - 10:10	39.9 - 38.8	864 - 867	113	A.1
2	2022-06-07	10:00 - 10:30	38.7 - 38.9	857 - 859	112	A.2
3	2022-06-21	09:50 - 10:25	38.0 - 38.5	837 - 839	113	A.3
4	2022-08-08	10:45 - 11:25	45.5 - 46.2	817 - 820	108	A.4
5	2022-08-09	10:15 - 10:45	45.6 - 45.8	823 - 824	108	A.5
6	2022-08-09	12:45 - 13:15	52.0 - 54.2	780 - 793	101	A.6

As seen from Table 3.1, the direct solar irradiance for the measurement sessions was roughly between 780 - 870 $\frac{W}{m^2}$, which is quite close to the AM1.5D standard irradiance of 900 $\frac{W}{m^2}$. The spectra in Appendix A show the differences in the simulated solar spectra between the sessions. The spectral differences occur due to differences in the solar zenith angle and atmospheric parameters, most importantly the total precipitable water (TPW) value. However, the measurement sessions' spectral differences against the AM1.5D standard are subtle enough that the spectral mismatch factor for each session remained between 0.90 and 1.02, as will be later shown in Section 3.1.4.

As an example, Figure 3.4 shows the simulated local solar spectrum plot for the first measurement session. The spectrum is plotted in terms of photon flux for better visibility of differences against the AM1.5D standard spectrum. It can be seen that the simulated

spectrum for the first session is a very close fit to the AM1.5D spectrum at UV and visible ranges. For the infrared wavelengths, there are some slight differences in the spectrum when compared to the standard. The photon flux at the most significant water absorption bands near 900, 1100 and 1400 nm are less attenuated than for the standard spectrum. This suggest that the local TPW value of the atmosphere for the session was less than that specified for the AM1.5D standard. Other sessions had a closer match to the AM1.5D standard near the water absorption bands, examples of which can be seen in Figure A.3 and Figure A.4 for sessions 3 and 4 respectively.

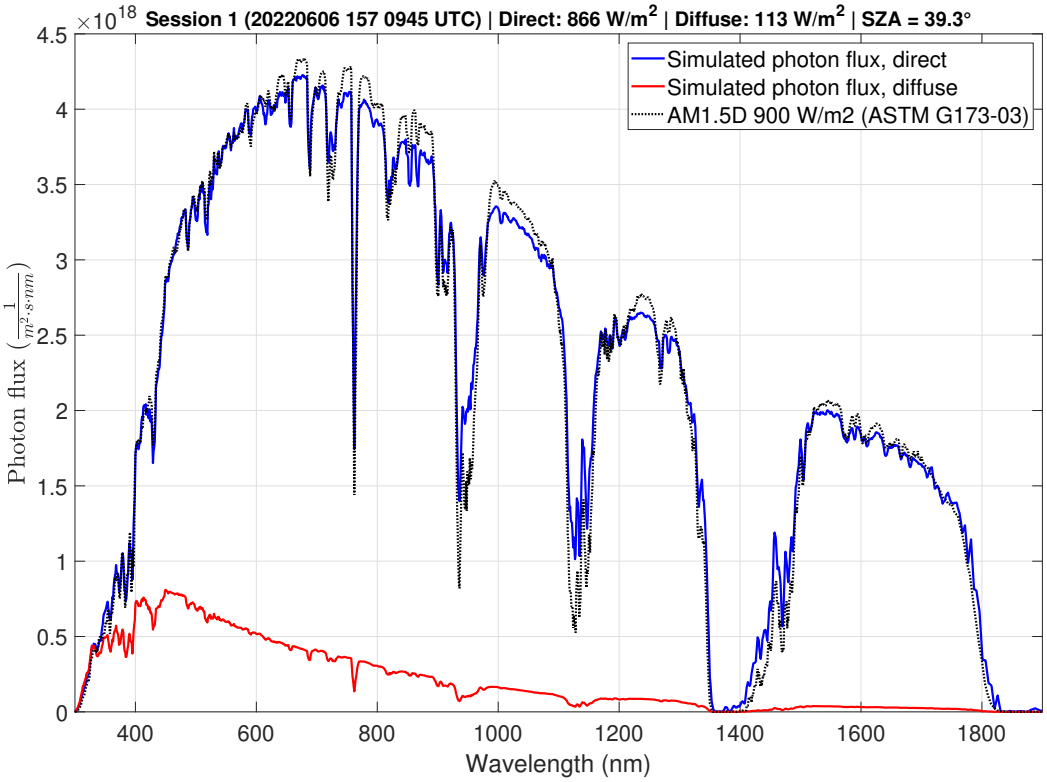

Figure 3.4. *Simulated photon flux spectrum for Session 1. Blue line is the simulated direct photon flux, and red line is the simulated diffuse photon flux. Black dotted line is the AM1.5D 900* $\frac{W}{m^2}$ *standard spectrum.*

3.1.3 Analysis of outside measurement data

The simulated spectral data was provided in units of irradiance. However, for calculating and analyzing the current generation of solar cells, a more suitable unit for the spectral data is the photon flux. Therefore, the spectral irradiance $I(\lambda)$ ($\frac{W}{m^2}$) was converted to spectral photon flux $\Phi(\lambda)$ ($\frac{1}{m^2 s}$) by

$$\Phi(\lambda) = \frac{I(\lambda)}{E_{phot}(\lambda)} = \frac{\lambda I(\lambda)}{hc}, \tag{3.1}$$

where $E_{phot}(\lambda)$ is the photon energy, c is the speed of light, and h is the Planck's constant.

Notation (λ) emphasizes the wavelength-dependence of the physical quantities, and the calculation is performed for each wavelength band separately with a resolution of 1 nm.

The samples were oriented perpendicular to the Sun during the measurements. The simulated spectral data was however provided for a horizontal surface (flat ground), so the direct photon flux has to be calculated for a perpendicular surface by simple geometrical relation

$$\Phi_{dir,p}(\lambda) = \frac{\Phi_{dir,h}(\lambda)}{cos(\theta_z)}, \tag{3.2}$$

where $\Phi_{dir,p}(\lambda)$ and $\Phi_{dir,h}(\lambda)$ are the direct photon fluxes for perpendicular and horizontal surfaces, respectively.

The External Quantum Efficiency (EQE) of each sample was used to analyze the spectral photon flux within the active range of each sample. Equation 2.10 was used to calculate the total current density under the incident spectrum by integrating the EQE over the spectral photon flux

$$J_{sc,EQE} = q \int_{\lambda_{min}}^{\lambda_{max}} EQE(\lambda) \cdot \Phi_{dir,p}(\lambda) \cdot d\lambda, \tag{3.3}$$

Notation $J_{sc,EQE}$ is used to emphasize that the current density is integrated from the EQE as opposed to a real-sun measurement. This distinction is important because the EQE-derived and real-sun values of J_{sc} can differ from each other due to many reasons explained in Section 2.3.4.

Spectral mismatch is a commonly used parameter to compare the current-generation performance of a solar cell between different incident spectra. The solar cell sample-specific spectral mismatch MM can be calculated in this case as the ratio of the current densities calculated from Equation 3.3

$$MM = \frac{J_{sc,EQE}(spectrum\,1)}{J_{sc,EQE}(spectrum\,2)} = \frac{\int_{\lambda_{min}}^{\lambda_{max}} EQE(\lambda) \cdot \Phi_{dir,p,1}(\lambda) \cdot d\lambda}{\int_{\lambda_{min}}^{\lambda_{max}} EQE(\lambda) \cdot \Phi_{dir,p,2}(\lambda) \cdot d\lambda}, \tag{3.4}$$

where $\Phi_{dir,p,1}$ and $\Phi_{dir,p,2}$ are the spectral photon fluxes of the two spectra in comparison.

The spectral mismatch (MM) is then used to extrapolate the outside measurement data to the predicted current density under the ASTM standard spectra [13] [12]. The accuracy of this extrapolation is proportional to the difference between the photon fluxes of the spectra. For this reason, the measurements were performed when the outside solar spectrum was closest similar to the AM1.5D spectrum, which is the main target calibration spectrum of this thesis. The current density under the AM1.5D standard spectrum $J_{sc,AM1.5D}$ is extrapolated from the measured outside real-sun value $J_{sc,real}$ by

$$J_{sc,AM1.5D} \approx MM \cdot J_{sc,real} = \frac{J_{sc,EQE}(AM1.5D)}{J_{sc,EQE}(real\text{-}sun)} \cdot J_{sc,real} \tag{3.5}$$

The same Equation 3.5 can be used to predict the current density under any standard spectrum, however it is most accurate for the AM1.5D calibration. The calibration could be done directly by using the real-sun current density $J_{sc,real}$, which can be thought of as copying the day's sunshine to the laboratory. For standard spectrum calibration however, this slight correction to the current density is required to account for the spectral mismatch. In the measurement dataset, the spectral mismatch to the AM1.5D standard spectrum was between 0.90 and 1.02, which translates to a very reasonable extrapolation.

Standard solar cell measurements are performed under sample temperature of 25 °C. In the outside measurements, the temperature of the samples was approximately constant over each measurement session. Different sessions had sample temperatures between 28 °C and 33 °C. The temperature dependence of the short-circuit current of solar cells made from similar III-V materials has been studied to be around 0.005-0.006 $mA/cm^2/C$ [45][46]. A simple approximation shows that the maximum temperature-induced error for the current density can vary roughly from 0.02 mA/cm^2 to 0.05 mA/cm^2 in comparison to standard 25 °C. Relative error in current density is then small fractions of a percent, which is why temperature-related effects are neglected in this thesis. For temperature differences of more than 10 °C, this effect becomes more significant and the current densities should be corrected with the sample-specific current-temperature coefficients.

All the calculations presented in this Chapter were performed using custom Matlab scripts. The complete data analysis path is illustrated in Figure 3.5. The input data was the measured EQE curve, outside measurement current density with 5.8° circumsolar angle, the local simulated spectrum for the measurement time with a 5 minute resolution, and the target standard spectrum. Because the outside measurements were performed through a fused silica (FS) window, also the calculation for $J_{sc,EQE}$ included the optical loss related to the window. For this calculation, the optical transmittance of the FS window was measured with PerkinElmer Lambda 1050 spectrophotometer, which was roughly 93-94% between 300-1800 nm as presented in Figure 3.6.

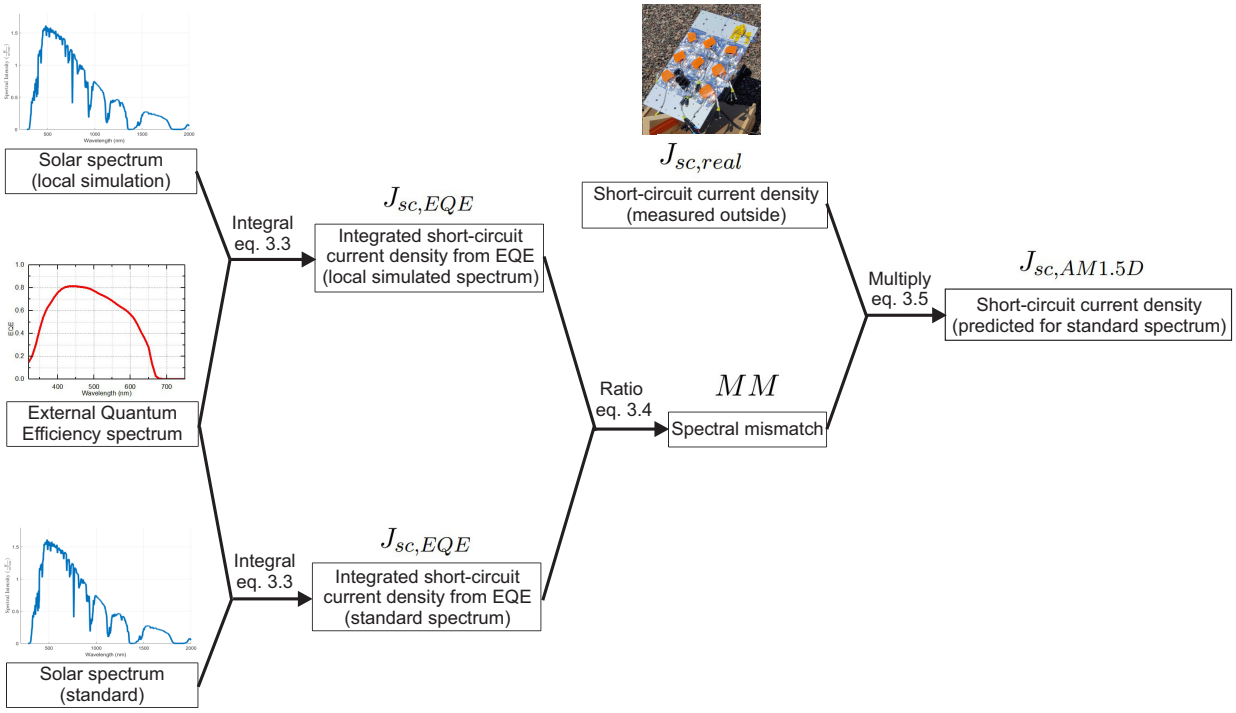

Figure 3.5. *Data analysis path for calculating the predicted calibration short-circuit current density for a sample.*

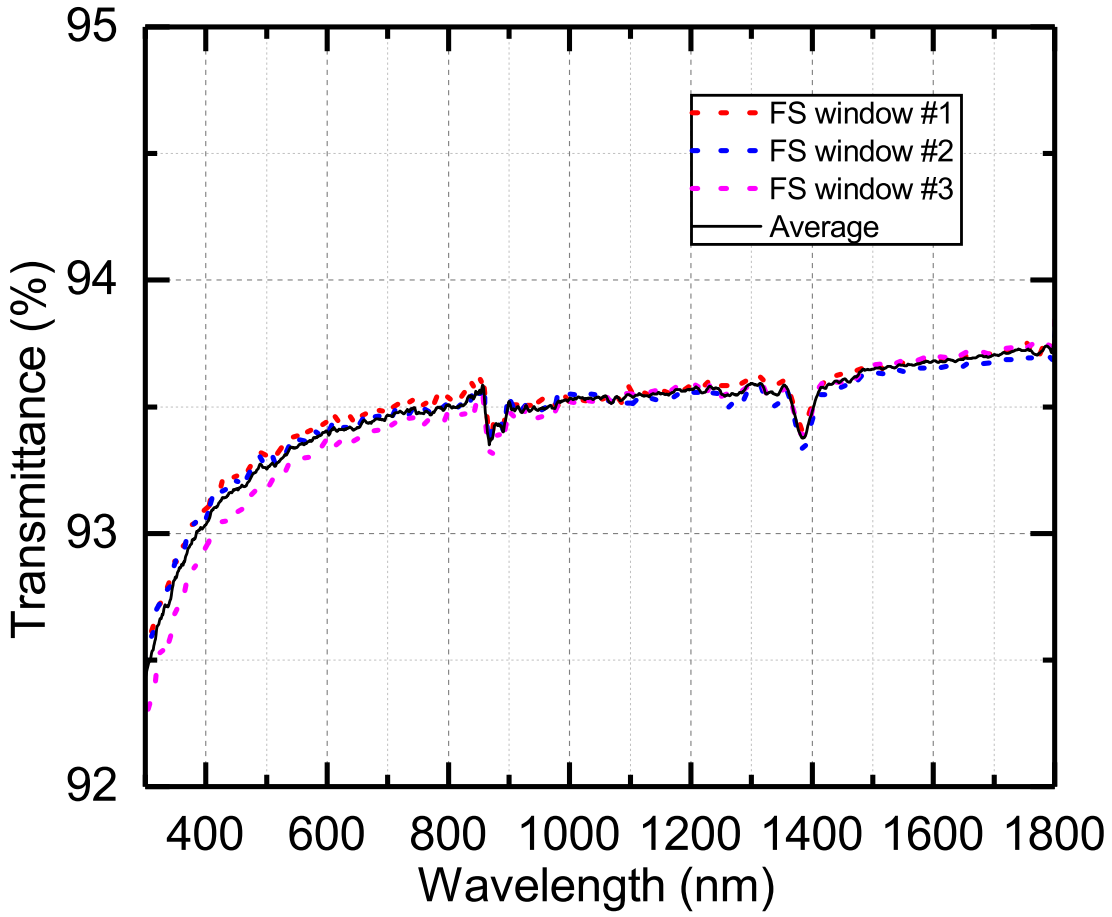

Figure 3.6. *Transmittance of the fused silica (FS) window through which outside measurements were performed. Measurement from three different samples shows very little variance between windows.*

3.1.4 Final calibration data

The calculated calibration data for AM1.5D spectrum is presented in Table 3.2 and visualized in Appendix B. The same calculations were performed for AM1.5G and AM0 spectra, with the final summary presented in Table 3.3.

Table 3.2. *Calculated AM1.5D calibration values for each sample. All the values in the table include a thin FS window placed on top of the cell. AM1.5D spectrum used according to standard ASTM G173-03(2020) [12]. Data is visualized in Appendix B.*

Sample ID	Session #	$J_{sc,real}$ mA/cm^2	$J_{sc,EQE}$ mA/cm^2	Mismatch AM1.5D 900 W/m^2	Predicted J_{sc} AM1.5D 900 W/m^2	Predicted J_{sc} AM1.5D 1000 W/m^2
1(690)	1	9.77	8.86	0.996	9.81	10.90
1(690)	2	9.76	8.88	0.999	9.77	10.86
1(690)	3	9.87	8.88	0.998	9.89	10.98
1(690)	4	9.30	8.51	0.956	9.73	10.81
1(690)	5	9.82	8.53	0.959	10.24	11.38
1(690)	6	9.17	8.00	0.899	10.21	11.34
2(900)	1	8.35	7.77	0.988	8.45	9.39
2(900)	2	8.27	7.75	0.986	8.39	9.32
2(900)	3	8.28	7.67	0.975	8.49	9.44
2(900)	4	8.08	7.52	0.957	8.44	9.38
2(900)	5	8.40	7.55	0.961	8.74	9.71
2(900)	6	8.16	7.30	0.928	8.80	9.77
3(900)	1	9.34	8.72	0.989	9.44	10.49
3(900)	2	9.20	8.70	0.986	9.33	10.36
3(900)	3	9.26	8.61	0.976	9.48	10.54
3(900)	4	8.97	8.44	0.957	9.37	10.41
3(900)	5	9.37	8.48	0.961	9.74	10.83
3(900)	6	9.02	8.18	0.928	9.72	10.80
4(1310)	1	7.33	7.01	1.021	7.18	7.98
4(1310)	2	7.13	6.86	0.999	7.13	7.93
4(1310)	3	7.03	6.54	0.953	7.38	8.19
4(1310)	4	6.96	6.51	0.948	7.34	8.15
4(1310)	5	7.28	6.59	0.960	7.59	8.43
4(1310)	6	7.02	6.41	0.934	7.51	8.35
5(1610)	1	-	-	-	-	-
5(1610)	2	-	-	-	-	-
5(1610)	3	24.12	22.98	0.953	25.31	28.12
5(1610)	4	24.57	22.79	0.945	26.00	28.88
5(1610)	5	25.20	23.05	0.956	26.37	29.30
5(1610)	6	24.76	22.36	0.927	26.71	29.68
6(1610)	1	-	-	-	-	-
6(1610)	2	-	-	-	-	-
6(1610)	3	23.46	22.10	0.953	24.61	27.34
6(1610)	4	22.84	21.92	0.945	24.16	26.84
6(1610)	5	23.49	22.16	0.956	24.58	27.31
6(1610)	6	22.92	21.50	0.927	24.71	27.46

Table 3.3. *Summary of calibration current density values. Calculated including a thin FS window in beam path. Standard deviation included. Current density units* mA/cm^2.

Sample ID	Predicted J_{sc} AM1.5D 1000 W/m^2	Predicted J_{sc} AM1.5G 1000 W/m^2	Predicted J_{sc} AM0 1366 W/m^2
1(690)	11.05 $\pm$ 0.25	11.64 $\pm$ 0.27	15.00 $\pm$ 0.34
2(900)	9.50 $\pm$ 0.19	9.42 $\pm$ 0.19	10.69 $\pm$ 0.21
3(900)	10.57 $\pm$ 0.20	10.49 $\pm$ 0.20	11.95 $\pm$ 0.22
4(1310)	8.17 $\pm$ 0.20	7.86 $\pm$ 0.19	9.67 $\pm$ 0.24
5(1610)	29.00 $\pm$ 0.67	27.91 $\pm$ 0.64	36.35 $\pm$ 0.84
6(1610)	27.24 $\pm$ 0.27	26.24 $\pm$ 0.26	33.93 $\pm$ 0.34

3.1.5 Comparison with direct EQE calibration

For comparison, the calibration current density values for the standard spectra were also directly calculated by integrating the EQE by Equation 3.3. Comparison of calibration targets calculated by the thesis method and the direct EQE integral is presented in Figure 3.7.

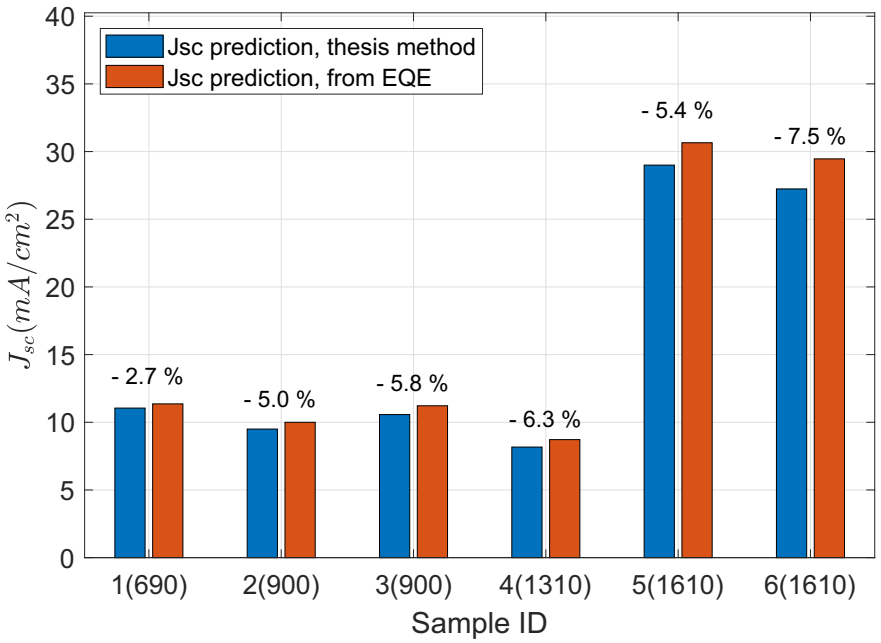

Figure 3.7. *Comparison of calibration target current density values for AM1.5D 1000* W/m^2 *spectrum. Thesis method vs. directly integrating from EQE.*

Figure 3.7 shows that the current density target values calculated by the thesis method are between 2 - 8 % smaller than those directly integrated from the EQE. This margin likely includes systematic error components as well as random error components, which can arise from EQE system calibration, uncertainty in the cell area, or sample non-uniformity, for example.

The solar cell current density is often approximated as linearly proportional to the incident photon flux, however the small-signal EQE measurement and one-sun IV measurement can have a difference of orders of magnitude in the photon flux which may slightly break this approximation and introduce errors. In comparison, the thesis method builds on the real-sun measurements with mismatch of 0.90 - 1.02 to the AM1.5D irradiance spectrum, which makes for a much more accurate extrapolation of current density compared to the EQE-integral method. In summary, the data shows that the EQE-integrated current density can be used for a rough first approximation, with arguably more precise results being achieved by the thesis method.

3.2 Solar simulator calibration experiments

Calibration tests were performed for two solar simulators: the OAI Trisol simulator and the G2V Pico simulator, which are later referred to as *Trisol* and *Pico*. The calibration goal for the experiment was to match the predicted current density values for standard spectra in Table 3.3. The calibration process was started for both simulators from the short end of the wavelength spectrum.

3.2.1 Xenon arc solar simulator (OAI Trisol)

The Trisol calibration was measured using a four-point probing setup and the six different calibration samples. A fused silica (FS) window was placed in the path of the incident light similarly as in the outside measurements. Sample temperature was stabilized to 25 ℃ with a thermoelectric controller. The probing setup is pictured in Figure 3.8.

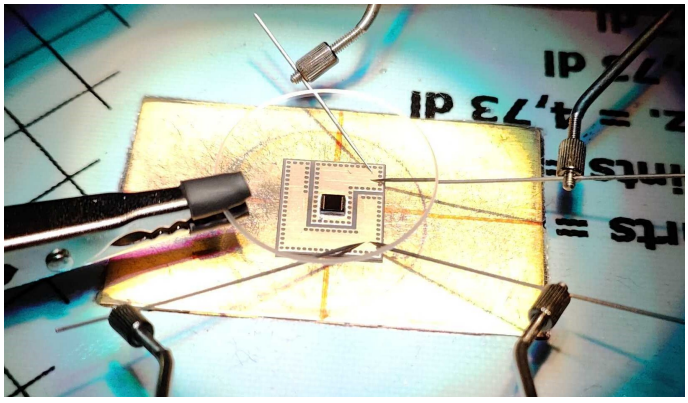

Figure 3.8. *The sample setup for the calibration measurements, including a fused silica window in beam path.*

As mentioned in Section 2.2.2, the Trisol simulator has very limited spectral tunability. The spectrum and irradiance on the working surface can be adjusted by three different means: by adjusting the lamp current, by changing the air mass (AM) filter, and by changing the neutral density (ND) filter. In one-sun operation mode, the ND filter slot is left empty to reach the required irradiance. The lamp current was adjusted to match the calibration current density for sample 1(690) from Table 3.3. Then the other calibration samples were measured with the same lamp current and settings. The calibration was performed with the AM1.5 and AM0 optical filters for the respective standard spectra. Calibration results for the Trisol simulator are presented in Table 3.4, Table 3.5 and Table 3.6.

Table 3.4. *Summary of Trisol simulator calibration test for AM1.5D 1000 W/m^2 spectrum. Measured using the AM1.5 filter. Target current density values from Table 3.3. Units mA/cm^2.*

Sample ID	Target J_{sc} AM1.5D 1000 W/m^2	Measured J_{sc} OAI Trisol simulator	Error Measured J_{sc} / Target J_{sc}
1(690)	11.05	11.07	+ 0.2 %
2(900)	9.50	13.34	+ 40.4 %
3(900)	10.57	14.63	+ 38.4 %
4(1310)	8.17	10.55	+ 29.1 %
5(1610)	29.00	44.98	+ 55.1 %
6(1610)	27.24	42.75	+ 57.0 %

Table 3.5. *Summary of Trisol simulator calibration test for AM1.5G 1000 W/m^2 spectrum. Measured using the AM1.5 filter. Target current density values from Table 3.3. Units mA/cm^2.*

Sample ID	Target J_{sc} AM1.5G 1000 W/m^2	Measured J_{sc} OAI Trisol simulator	Error Measured J_{sc} / Target J_{sc}
1(690)	11.64	11.74	+ 0.9 %
2(900)	9.42	14.13	+ 33.3 %
3(900)	10.49	15.37	+ 31.7 %
4(1310)	7.86	11.16	+ 29.6 %
5(1610)	27.91	47.17	+ 40.8 %
6(1610)	26.24	45.17	+ 41.9 %

Table 3.6. *Summary of Trisol simulator calibration test for AM0 1366 W/m^2 spectrum. Measured using the AM0 filter. Target current density values from Table 3.3. Units mA/cm^2.*

Sample ID	Target J_{sc} AM0 1366 W/m^2	Measured J_{sc} OAI Trisol simulator	Error Measured J_{sc} / Target J_{sc}
1(690)	15.00	14.61	- 2.6 %
2(900)	10.69	12.80	+ 19.8 %
3(900)	11.95	14.66	+ 22.7 %
4(1310)	9.67	15.28	+ 58.0 %
5(1610)	36.35	54.26	+ 49.3 %
6(1610)	33.93	51.60	+ 52.1 %

From the Trisol calibration results for AM1.5D spectrum in Table 3.4, it is observed that when the lamp current is calibrated with sample 1(690) to match current density in the

UV and visible ranges, the current density values in the infrared range are up to 50-60% greater than the target. In other words, the simulator spectrum is significantly weighted towards the infrared wavelengths. Similarly, the AM1.5G and AM0 spectra calibration results in Table 3.5 and Table 3.6 show major imbalance up to 42% and 58 % respectively for the current densities. Based on this experiment, the Trisol simulator does not match the A class requirements for spectral match though it has been characterized in class A by the manufacturer in 2016. Many factors might have affected the spectral match since, with the most significant effect resulting from the replacements and aging of the xenon arc lamps which have been observed to red-shift over hundreds of usage hours. Unfortunately, there is no simple way to combat this spectral shift with such limited adjustment options.

3.2.2 Multi-channel LED simulator (G2V Pico)

The Pico calibration measurement was performed with the same setup as for the Trisol, using a four-point probing setup and the six different calibration samples. A fused silica (FS) window was placed in the path of the incident light similarly as in the outside measurements. Sample temperature was stabilized to 25℃ with a thermoelectric controller.

As mentioned in Section 2.2.2, the Pico simulator has 32 adjustable wavelength channels in the range 350 - 1500 nm. This allows for much more calibration flexibility and accuracy than for the Trisol simulator. The calibration current densities were matched one-by-one, starting from the shortest wavelength sample 1(690). The power of LED channels in the active wavelength range of the sample were adjusted systematically until the current density matched the target. Then, the current density was matched for the next sample 2(900) by adjusting the power of LED channels between roughly 690 nm and 900 nm. This way, the current density for sample 2(900) can be matched to target while having minimal effect on the current density of sample 1(690). The same procedure was performed for all samples in order of increasing band gap wavelength. The only exception from the procedure was for the samples 5(1610) and 6(1610), for which also the LED wavelength band at 870 nm to 970 nm was adjusted. This was decided as necessary because the other samples had such low EQE response at 870 nm to 970 nm that it was not enough for accurate calibration. However, samples 5(1610) and 6(1610) have their maximum EQE response of about 0.8 to 0.9 there which allowed for calibrating this wavelength "gap". Some extra attention was also required to match the irradiance at the most significant water absorption bands at about 950 nm, 1100 nm and 1400 nm, which correspond to the irradiance "valleys" in the AM1.5D and AM1.5G spectra in Figure 2.4.

After all six samples were calibrated, the LED current readings were saved to a spectrum file, and then all the samples were measured again with this saved spectrum. It was clear that during the adjustment process, the current density for previous samples would also change due to some of the LED spectra overlapping with multiple samples' EQE spectrum. In addition, any larger adjustment of LED power within the LED array will

affect the temperature profile of the array, potentially affecting the emission properties of also those LED's whose current was not adjusted. For these reasons, it was necessary to re-iterate the whole calibration process for up to three times to finally match the calibration current density targets within an error margin of 0-2 %. The calibration process flow is illustrated in Figure 3.9. The calibration results for the G2V Pico are presented in Table 3.7, Table 3.8 and Table 3.9 for the AM1.5D, AM1.5G and AM0 spectra, respectively. The main calibration target for the research requirements was the AM1.5D spectrum, however with the thesis method it was very straightforward to also perform calibrations for the AM1.5G and AM0 spectra.

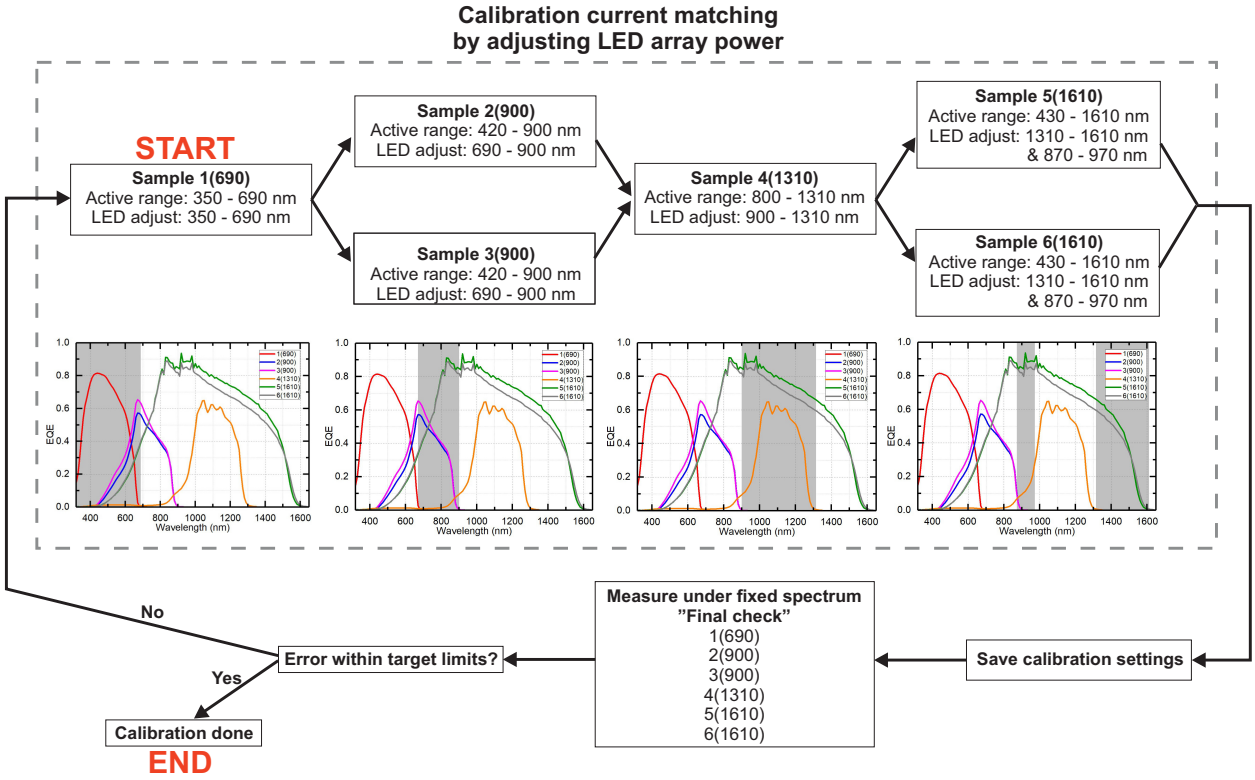

Figure 3.9. *The calibration process flow for the Pico solar simulator.*

Table 3.7. *Summary of Pico simulator calibration test for AM1.5D 1000 W/m^2 spectrum. Target current density values from Table 3.3. Units mA/cm^2.*

Sample ID	Target J_{sc} AM1.5D 1000 W/m^2	Measured J_{sc} Pico simulator	Error Measured J_{sc} / Target J_{sc}
1(690)	11.05	11.07	+ 0.2 %
2(900)	9.50	9.51	+ 0.1 %
3(900)	10.57	10.56	- 0.1 %
4(1310)	8.17	8.16	- 0.1 %
5(1610)	29.00	28.90	- 0.4 %
6(1610)	27.24	27.42	+ 0.7 %

Table 3.8. *Summary of Pico simulator calibration test for AM1.5G 1000 W/m^2 spectrum. Target current density values from Table 3.3. Units mA/cm^2.*

Sample ID	Target J_{sc} AM1.5G 1000 W/m^2	Measured J_{sc} Pico simulator	Error Measured J_{sc} / Target J_{sc}
1(690)	11.64	11.66	+ 0.1 %
2(900)	9.42	9.44	+ 0.3 %
3(900)	10.49	10.49	+ 0.0 %
4(1310)	7.86	7.88	+ 0.3 %
5(1610)	27.91	27.78	- 0.5 %
6(1610)	26.24	26.65	+ 1.5 %

Table 3.9. *Summary of Pico simulator calibration test for AM0 1366 W/m^2 spectrum. Target current density values from Table 3.3. Units mA/cm^2.*

Sample ID	Target J_{sc} AM0 1366 W/m^2	Measured J_{sc} Pico simulator	Error Measured J_{sc} / Target J_{sc}
1(690)	15.00	15.04	+ 0.3 %
2(900)	10.69	10.76	+ 0.7 %
3(900)	11.95	11.97	+ 0.2 %
4(1310)	9.67	9.70	+ 0.3 %
5(1610)	36.35	34.47	- 5.4 %
6(1610)	33.93	32.83	- 3.3 %

The calibration data for the Pico simulator in Table 3.7 and Table 3.8 shows that the calibration targets for each sample were reached within 0 - 1.5 % error for the AM1.5D and AM1.5G spectra. This can be considered as very good calibration accuracy for such a wide spectral range, especially when comparing against the results from the Trisol simulator in Section 3.2.1. In the AM0 spectrum calibration results in Table 3.9, the error from calibration targets remains less than 1% for wavelengths between 300 nm and 1300 nm, however for the last two samples 5(1610) and 6(1610) the current is 3-6% less than the target. This larger error for AM0 in infrared between 1300 nm and 1600 nm occurs for two reasons. The LED's at 1300 nm to 1500 nm were operating at their maximum power, which was not enough for the infrared irradiance required in AM0 spectrum. In addition, there are no LED's allocated for the range 1500 nm to 1600 nm, a band at which the samples 5(1610) and 6(1610) have some active EQE response. In comparison, the AM1.5D and AM1.5G targets were reached quite conveniently without hitting the maximum power limits of the LEDs at infrared wavelengths.

The Pico software shows a plot of the spectral irradiance in the user interface. This irradiance spectrum is not measured in real-time, and is rather an approximation from the superposition of the individual LED's in the LED array. The approximated LED spectra

are presented in Figure 3.10. Though the ultraviolet peaks at 350 - 400 nm seem overly intense in Figure 3.10, in Figure 3.11 it is more clearly seen that the gaps in between the peaks will compensate for the somewhat excessive peak intensities in the overall integrated irradiance.

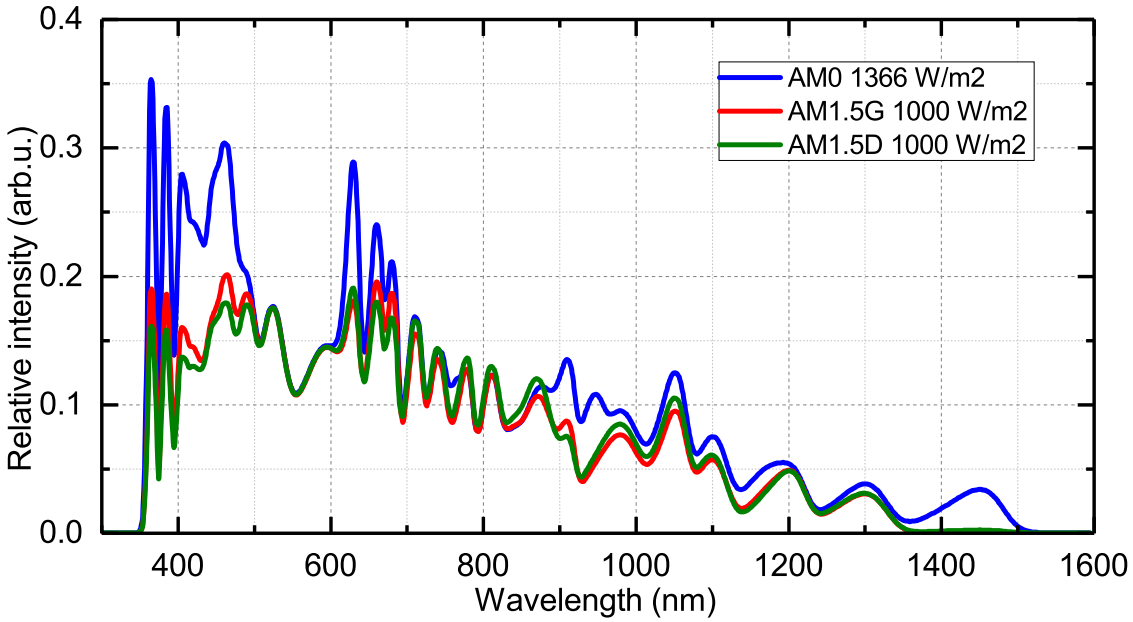

Figure 3.10. *Calibration spectra approximations obtained from the Pico software.*

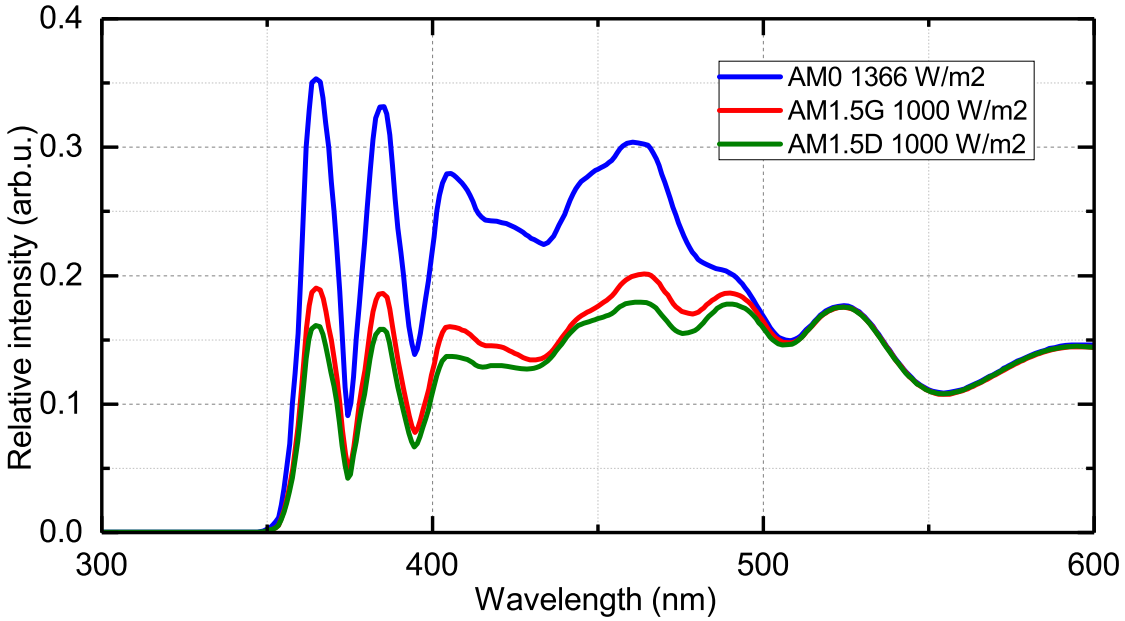

Figure 3.11. *Calibration spectra approximations obtained from the Pico software. X-axis narrowed to show artifact at 350 - 400 nm.*

Comparison of the Pico calibrated AM1.5D spectra and the AM1.5D standard [12] is pre-

sented in Figure 3.12. The LED spectrum approximation matches the AM1.5D standard spectrum quite well, even including the water absorption valleys near 950 nm, 1100 nm and 1400 nm. There are no LED's at 300 to 350 nm, which is why the irradiance is slightly overshot at about 350 - 450 nm to compensate in the total irradiance. Similarly, due to the lack of LED's with emission peak at 550 to 600 nm, the spectrum has a slight valley there which is again compensated in the adjacent wavelength bins. Also, the Pico's LED array has maximum wavelength at about 1500 nm, leaving effectively zero irradiance for wavelengths longer than 1500 nm. This is also compensated by slight adjustments to the adjacent wavelength bins.

Overall, it is clear that the AM1.5D LED spectrum of Figure 3.12 has a more "wavy" or comb-like fine structure from the individual LED power peaks. However, in the calibration the overall photon fluxes in the spectral bands are matched, which basically means that the LED spectrum will average out closer to the standard spectrum i.e. their integrals are matched. In summary, though the LED spectrum is an approximation and does have slight differences to the standard spectrum, it is nevertheless a good spectral match and qualitatively confirms the high accuracy of the calibration results for the AM1.5D spectrum in Table 3.7.

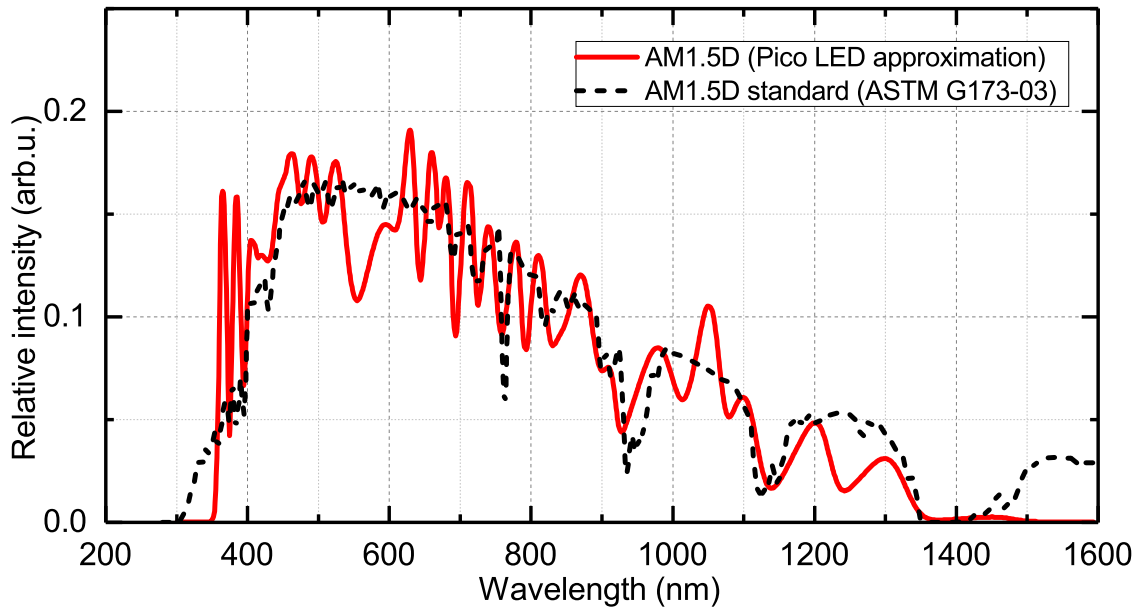

Figure 3.12. *Spectral approximation for the AM1.5D 1000 W/m^2 calibration of the Pico solar simulator.*

Figure 3.13 shows a comparison of the Pico calibrated AM1.5G spectra and the AM1.5G standard [12]. The AM1.5G spectrum is quite similar to the AM1.5D spectrum when both are normalized to total irradiance of 1000 W/m^2. The main difference is that the AM1.5G ("global") spectrum is slightly more intense in the UV and visible ranges, while for the infrared range at >700 nm the AM1.5D ("direct") spectrum has more irradiance as discussed in Section 2.1. This spectral balance is visible in the standard spectra of Figure

2.1 and is repeated in the LED spectra of Figure 3.10. Overall, the AM1.5G LED spectrum very similar features as the AM1.5D LED spectrum discussed above, again qualitatively confirming the high accuracy of the calibration results for the AM1.5G spectrum in Table 3.8.

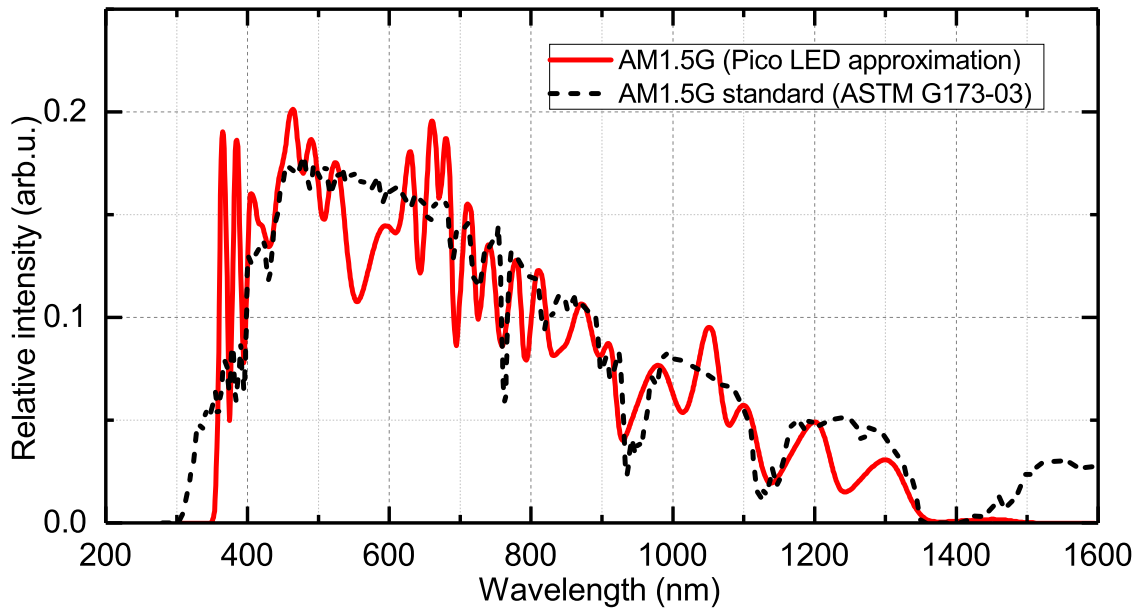

Figure 3.13. *Spectral approximation for the AM1.5G 1000 W/m^2 calibration of the Pico solar simulator.*

Figure 3.14 shows a comparison of the Pico calibrated AM0 spectra and the AM0 standard [13]. Clearly, there is more variation from the target spectrum when compared to what was achieved for the AM1.5D and AM1.5G spectra. First, the AM0 target spectrum has much more irradiance in the UV range below 350 nm where the LED spectrum cannot reach. This leads to large overshooting required at 350 nm to 450 nm to compensate in total irradiance. Also, the LED infrared irradiance over 1100 nm is less than the AM0 target, a fact which was already observed from calibration results in Table 3.9 where the samples 5(1610) and 6(1610) were generating roughly 3-6 % less current than the target. The valley between 500 nm and 600 nm is relatively more significant for the AM0 calibration, requiring strong compensation by overshooting the irradiance in the adjacent bands. Overall, while the LED spectrum does have wide resemblances to the AM0 standard spectrum, it is not as good a spectral match as the AM1.5D and AM1.5G calibrations. Similar conclusion can be made from the calibration current density Table 3.9.

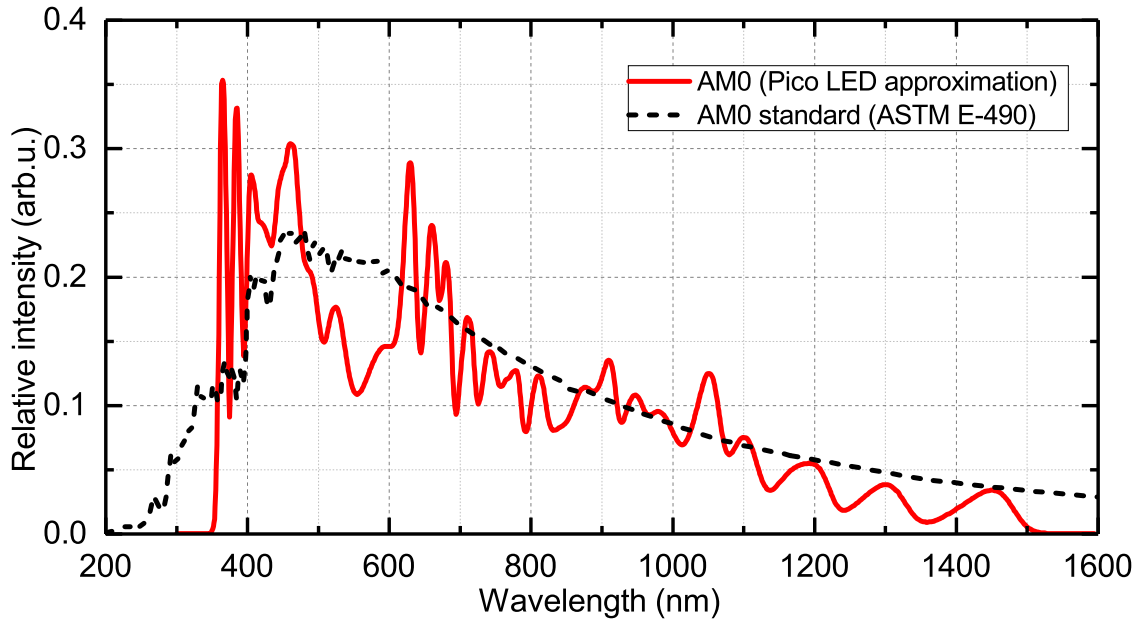

Figure 3.14. *Spectral approximation for the AM0 1366 W/m^2 calibration of the Pico simulator.*

The spectral valley between 550 and 600 nm is directly related to the *green-yellow gap*, which refers to the lack of high-power LED's available at this wavelength range [47]. This affects the AM0 LED spectrum quite strongly, with the irradiance valley seemingly extending also towards green wavelengths at 500 nm to 550 nm. Fortunately, the green-yellow gap has a smaller effect for the AM1.5D and AM1.5G spectra, which were the most important calibration targets of this thesis. The spectral range and available power of the LED array was clearly a better fit for the AM1.5D and AM1.5G spectra.

As discussed in Section 3.1.3, the thesis method is optimized to produce the most accurate and reliable calibration results for the AM1.5D spectrum. Similar accuracy can be expected for the AM1.5G spectrum due to its close resemblance with the AM1.5D spectrum. The tests show that the Pico simulator is a good fit for this calibration method. However, the results for the AM0 calibration are less accurate, with the calibrated spectrum showing a more distorted shape with respect to the target spectrum. The AM0 calibration could be improved by including extra light sources for boosting the green and yellow irradiance between 500 nm to 600 nm and the infrared irradiance above 1100 nm.

3.3 Calibration comparison with multi-junction solar cells

For each of the solar simulator calibration sessions in Chapter 3.1, multi-junction solar cell samples were also measured with under the same spectra. These measurements were performed to study the effect of the spectrum on the multi-junction solar cell characteristics. The target spectrum for these measurements was the AM1.5D standard spectrum [12]. The Pico calibration was matched to targets through the whole spectrum within 1% error as seen from the results in Table 3.7, which means that the Pico is precisely calibrated for the whole range from roughly 300 nm to 1600 nm. For the Trisol simulator, because the calibration current targets for the whole spectrum cannot be matched simultaneously, the spectrum will depend on which spectral range is chosen for the calibration. Therefore, to further analyze the effects of the spectral imbalance, the Trisol was calibrated two different ways. First Trisol measurement set was calibrated with the sample 1(690) in ultraviolet and visible ranges (UV-Vis) from 300 nm to 690 nm, which leads to a surplus of irradiance in the infrared. The second Trisol measurement set was calibrated with the sample 5(1610) in the infrared (IR) range from about 700 nm to 1600 nm, which conversely leads to a lack of irradiance in the UV and visible range. All the measurements were performed with a sample temperature of 25℃. The IV curves and measured performance parameters are presented in Figure 3.15 and Figure 3.16 for the 2J and 4J samples, respectively.

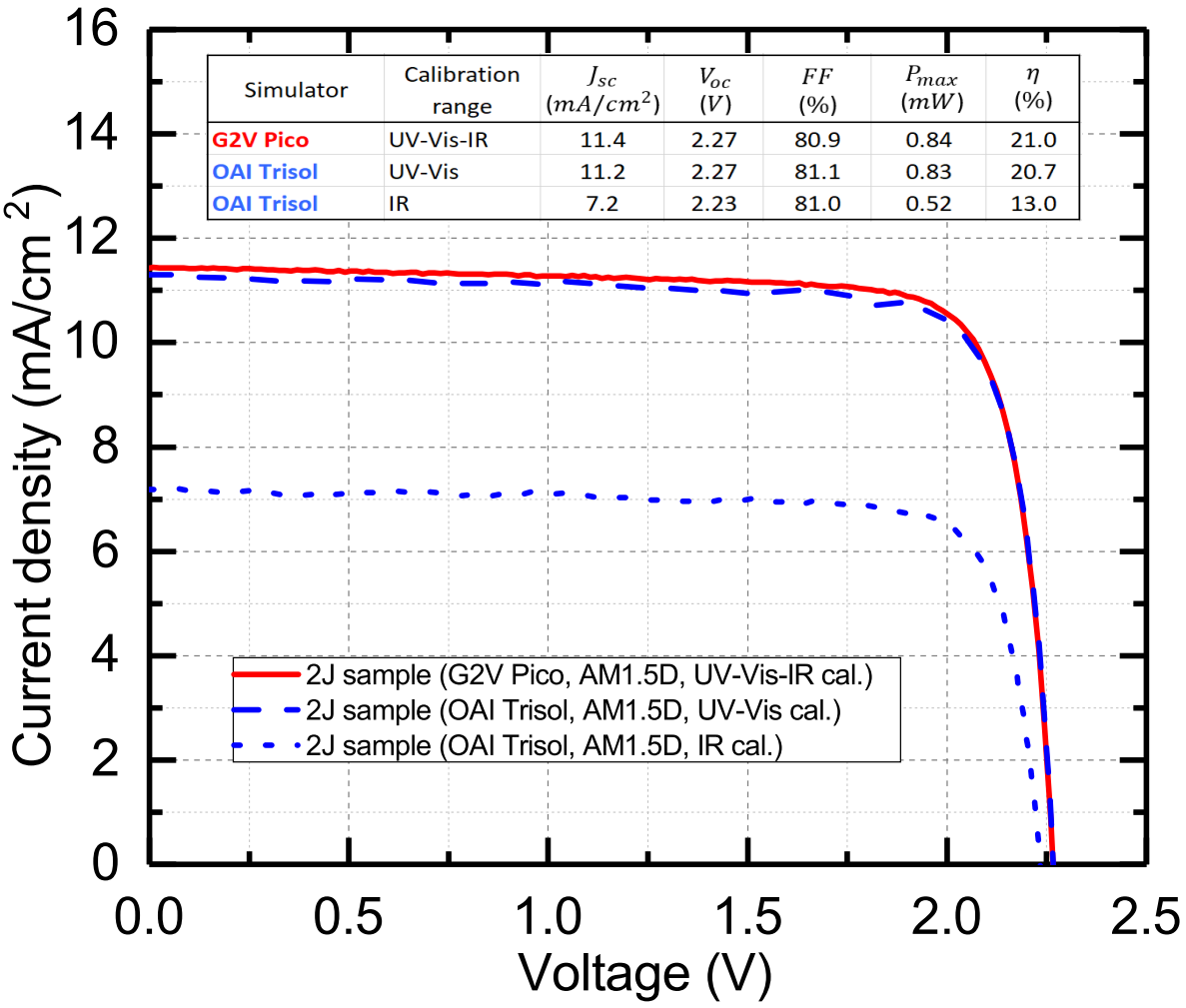

Figure 3.15. *Comparison of IV curve and performance parameters for the 2J sample under calibrated simulators. AM1.5D 1000 W/m^2 spectrum.*

Figure 3.15 shows that though the calibration target for all measurements was the same AM1.5D spectrum, the measured IV curves and performance parameters have some differences. When the Trisol simulator is calibrated for the UV and visible ranges, the measured IV curve for the 2J sample is very similar to that achieved with the Pico, with all performance parameters within 2% relative difference. This is because the 2J sample is current-limited by the top subcell which operates in the UV-Vis range and is very similar to the used calibration sample 1(690). Though there is a lot of extra irradiance in the IR range in the UV-Vis calibration, the extra irradiance has very little effect on the performance of the 2J sample. This is a good example that the sample performance can be very similar by "coincidence" though the Pico and Trisol spectra are very different.

On the contrary, when the Trisol is calibrated in the infrared (IR) range, the lack of irradiance in the UV-Vis range leads to a significantly smaller photocurrent for the top subcell and thus for the whole 2J sample. This contributes to the 37% decrease in current density and 38% decrease in power when compared to the results measured with the Pico. Based on these results, the Trisol produces largely varying characterization data depend-

ing on which part of the spectrum was calibrated, with the measured IV curves placing anywhere in between the dashed Trisol IV curves. The Pico produces results that are much more precise, reliable and repeatable due to the wide and accurate spectral calibration achieved in this thesis.

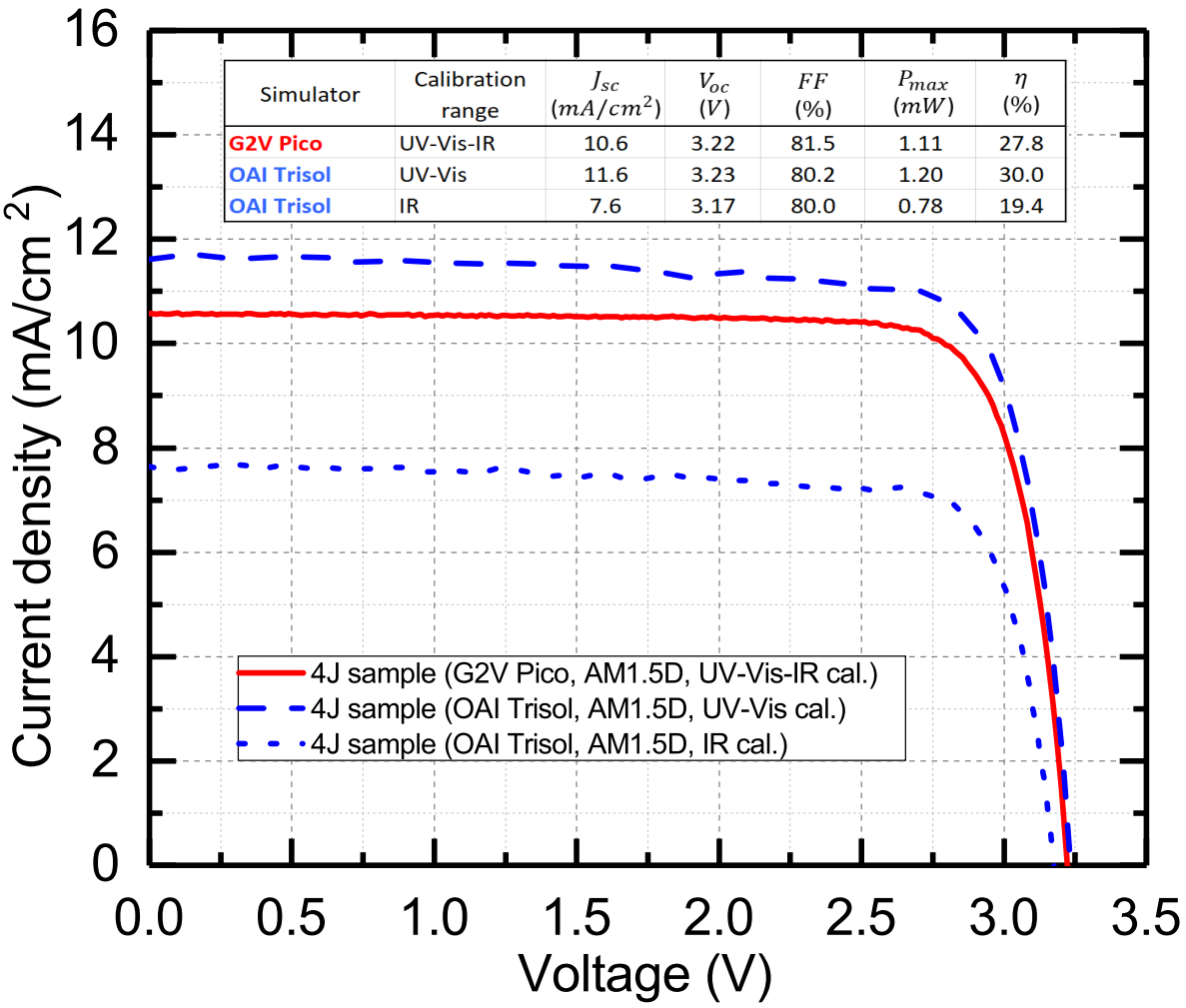

Figure 3.16. *Comparison of IV curve and performance parameters for the 4J sample under calibrated simulators. AM1.5D 1000 W/m^2 spectrum.*

Figure 3.16 shows again that though the calibration target was the same AM1.5D spectrum, the measured IV curves and performance parameters of the 4J sample have some significant differences. However, now the UV-Vis calibrated measurement for the Trisol contains a larger error about 10% in the current density, overestimating the photocurrent when compared to the measurement with the Pico. This suggests that the current-limiting subcell is not the top cell as was the case for the 2J sample. As a side note, it can be concluded that current-limiter in these measurements was the second subcell from the top which is made from gallium arsenide.

The IR calibration for the Trisol is again underestimating the 4J performance significantly, with up to 28% decrease in current density and up to 30% decrease in power of the 4J sample when compared to the Pico measurement. The variance of the measurement

results for the 4J sample with the Trisol are significant, in turn over- and underestimating the sample performance. Now, even the shape of the IV curve is affected by the different calibration between solar simulators, which is also seen in the decreased fill factor in the Trisol measurement.

These comparisons for the 2J and 4J samples underline the importance of the spectral calibration of the solar simulator. Spectral imbalances will produce unreliable and unpredictable results, with error margins often increasing as the number of junctions increase. This was already discussed in theory in Chapter 2.4.1 and is confirmed by the measurement results. As the calibrated spectral match to the AM1.5D standard spectrum for the Pico simulator was precise within 1% throughout the whole wavelength range, the results measured under the Pico illumination can be considered highly accurate. Though similar IV curves to the Pico can be measured with the Trisol, as in the 2J measurement of Figure 3.15, it will happen only by coincidence depending on the calibration. Most of the time, a relative error of more than 10-20% for the performance parameters can be expected for multi-junction measurements performed with the Trisol at its current state.

3.4 Analysis and discussion

The results of this thesis can be considered a successful demonstration of this new calibration method. The outside measurements were successfully performed in many sessions where the solar spectrum was close within 10% mismatch to the target AM1.5D standard spectrum, providing large amounts of performance data which was used in the calibration. The data analysis method is quite simple and scalable to many different samples.

The calibration targets from the data analysis were well matched with the Pico simulator within 1 % for the AM1.5D standard spectrum [12], which was the main target of this thesis. As a side result, the calibration targets for the AM1.5G spectrum were achieved within 2% error, and the AM0 spectrum targets within 6% error. Reflecting on the solar simulator spectral mismatch classes, these error margins are well within the A class specification of less than 25 %. The wide spectral adjustability of the Pico's LED array proved to be a good fit for the calibration method and its many different samples. The measurements of this thesis are also a good first test and benchmark for the Pico's tunability and stability. In addition, due to its use of LEDs, the calibrated Pico spectrum will remain constant for much longer lifetimes than the xenon arc lamps in the Trisol simulator which age significantly already after tens of usage hours according to the author's experience. By these results, the Pico will be replacing the Trisol in one-sun IV measurements in the solar cell research group at ORC, enabling highly accurate results with the calibration from this thesis.

The Trisol simulator calibration was not as successful, which was to be expected due to its lack of adjustment options. The spectral match class for the Trisol would be B or C based on these measurements. Most importantly, the Trisol measurements show that for this calibration method and for MJSC research, the xenon arc lamp and its lack of spectral tunability is often sub-optimal. This was already known beforehand, but is well emphasized in these results. The main benefit of the Trisol remains in its capability for providing high irradiance of up to 1500 suns in concentrated photovoltaic (CPV) measurements. As such, it will still be used at times for CPV measurements in the research group.

The thesis method utilizes real-sun measurements under illumination conditions which are very close to the standard spectrum, creating realistic and accurate calibration current targets. The thesis method avoids most of the uncertainties related to the direct EQE integral method because the absolute value of the EQE vanishes in the thesis calculation. Also, the thesis method removes any uncertainty related to the sample area because the same samples are used in both measurements of the calibration, outside and inside. Moreover, the outside IV measurement conditions are very similar to the solar simulator IV measurements, with only slight corrections required to account for the spectral mismatch. These can be considered as factors increasing the accuracy compared to the direct EQE integral method. When comparing the thesis method to standardized calibration with established calibration laboratory samples, the largest benefit is the cost-efficiency and

scalability as discussed in Section 3.1.

The most significant error source for the thesis calibration method is the uncertainty in the simulated spectrum. As discussed in Section 2.1.4, the accuracy for clear-sky radiative transfer simulation models can be expected to be within 3% under normal weather conditions. It is likely that this spectral uncertainty is the leading cause in the variance of the calibration current density values in Table 3.2, which have a standard deviation of roughly 2-3 % over the six real-sun sessions depending on the sample. The lack of temperature control for the sample in real-sun measurements is another potential error source, however its effect on the current density was approximated to be within a few tenths of a percent in Section 3.1.3. The incident light beam is slightly different when comparing the Sun outside and the LED array of the Pico, and the range of incidence angles in the Pico measurements was higher than in the direct measurement outside. The effect of the beam incidence was considered out of the scope of this.

Considering all the error sources in both the calibration target calculations and the calibration process, the accuracy of the results for the Pico simulator can be approximated to be between 5-10 %, which can be considered as a successful result as the target was a spectral match beyond the A class limits of $\pm$ 25%. A suitable next step in the development of this method would be more precise error analysis and cross-checking with results from established calibration laboratories. Increasing the amount of different calibration samples would further increase the spectral resolution and accuracy. Alternatively, the spectral resolution could be increased by including a suitable selection of optical shortpass and longpass filters in the measurements. Other improvements could be done by further optimizing the accuracy of the local spectrum simulations e.g. by including daily aerosol values in the simulation and cross-comparing with physical measurements of solar radiation. Adding extra light sources for the Pico setup in the ultraviolet, green-yellow and infrared wavelength ranges would allow for even wider spectral calibration and largely improved spectral match for the high intensity extraterrestrial AM0 spectrum.

4 SUMMARY

The target of this thesis research was to create and test a new calibration method for solar simulators. The calibration method was optimized to fulfill the requirements of multi-junction solar cell research at ORC with its main benefits including accuracy, spectral width and cost-effectiveness for large sample sets.

The outside measurements were performed during summer 2022 in Tampere, Finland. Arranging the measurements during mid-day hours on cloudless days of high solar irradiance proved to be a quite difficult task due to the unpredictability of the Finnish summer weather. Nevertheless, a good outside measurement dataset was gathered with a close spectral match to the AM1.5D standard spectrum over six measurement sessions. The outside measurement data was then converted into standard spectrum calibration data for the solar simulator. This extrapolation was performed from basis of the outside measurement data by using local simulated solar spectra for the measurement sessions and quantum efficiency measurement results. The data analysis of the method is straightforward and the close spectral match of the outside measurements supported the accuracy of the extrapolation by minimizing its magnitude.

The calibration target data from the outside data analysis was used to calibrate two solar simulators in the laboratory. For the LED-based G2V Pico solar simulator, the calibration process was a success within 1% final error margins from the AM1.5D calibration targets for the wavelength range from 300 nm to 1600 nm. For the AM1.5G and AM0 spectra calibrations, the error margins for the Pico simulator were within 2% and 6% respectively. The good spectral match to the AM1.5D and AM1.5G standard spectra was qualitatively confirmed by the calculated LED approximations. For the AM0 calibration, the LED spectrum was slightly more warped when compared to the standard spectrum, a result which is also reflected in the higher error margins. The LED-based Pico solar simulator proved to be a good fit for applying the thesis calibration method, with the best accuracy being achieved for the AM1.5D spectrum which was the main target spectrum of this thesis. The illumination spectrum of the Pico can be expected to remain constant for hundreds of usage hours due to its use of LED's, which are known to have great stability over long lifetimes when compared with arc lamps.

Another calibration was performed for a Xenon arc OAI Trisol solar simulator with the same calibration target data. As was expected, the calibrations for the Trisol had significantly higher inaccuracy of up to 57%, 42% and 58% for the AM1.5D, AM1.5G and AM0 spectrum calibrations, respectively. The irradiance spectrum of the xenon arc lamp

proved to be unfit for accurate multi-junction solar cell characterization. Additional difficulties arise from the significant observed red-shift of the Xenon arc lamp spectrum, which makes the calibration accuracy quickly disappear during the lamp lifetime. However, the Trisol simulator calibration provided a good comparison point to the Pico simulator calibration, emphasizing the importance of the choice of solar simulator for applying this calibration method. Comparison of a two-junction (2J) and four-junction (4J) solar cell performance under the two different simulators clearly showed the increased accuracy of the Pico simulator and the importance of a good calibration for multi-junction samples.

The LED-based G2V Pico solar simulator will be replacing the Xenon arc OAI Trisol simulator for performing one-sun solar cell measurements at the Optoelectronics Research Group. Combined with the calibration achieved in this thesis research, the setup is optimized to fulfill the requirements of multi-junction solar cell research due to its wide spectral accuracy and flexibility. The method can be further refined for greater spectral resolution and spectral band accuracy with negligible increases to the cost. In particular, improvements can be made by increasing the amount of different calibration samples and/or by including optical bandpass filters for spectral band selection. Extra lamps can be added to the Pico simulator in the ultraviolet, green-yellow and infrared ranges to allow for a wider spectral calibration and better match to the extraterrestrial AM0 spectrum. The simulation model for the local solar spectrum can be also be further modified to include more detail on the aerosol properties of the atmosphere, for example. Finally, the thesis calibration can be cross-compared with a similar calibration from an established calibration facility.

REFERENCES

[1] Green, M. A. "Silicon photovoltaic modules: a brief history of the first 50 years". *Progress in Photovoltaics* 13.5 (2005), 447–455.

[2] International Energy Agency: Photovoltaic Power Systems Programme. *"Snapshot of Global PV Markets 2022"*. URL: https://iea-pvps.org/snapshot-reports/snapshot-2022 (visited on 12/13/2022).

[3] PV Magazine International. *"World has installed 1TW of solar capacity"*. URL: https://www.pv-magazine.com/2022/03/15/humans-have-installed-1-terawatt-of-solar-capacity/ (visited on 12/13/2022).

[4] SolarPower Europe. *"Global Market Outlook For Solar Power 2022-2026"*. URL: https://www.solarpowereurope.org/insights/market-outlooks/global-market-outlook-for-solar-power-2022 (visited on 12/13/2022).

[5] Fraunhofer Institute for Solar Energy Systems ISE. *Photovoltaics Report 2022*. URL: https://www.ise.fraunhofer.de/en/publications/studies/photovoltaics-report.html (visited on 12/13/2022).

[6] Yoshikawa, K., Yoshida, W., Irie, T., Kawasaki, H., Konishi, K., Ishibashi, H., Asatani, T., Adachi, D., Kanematsu, M., Uzu, H. and Yamamoto, K. "Exceeding conversion efficiency of 26% by heterojunction interdigitated back contact solar cell with thin film Si technology". *Solar Energy Materials and Solar Cells* 173 (2017).

[7] Green, M. A., Dunlop, E. D., Siefer, G., Yoshita, M., Kopidakis, N., Bothe, K. and Hao, X. "Solar cell efficiency tables (Version 61)". *Progress in Photovoltaics: Research and Applications* 31 (2023).

[8] Baiju, A. and Yarema, M. "Status and challenges of multi-junction solar cell technology". *Frontiers in Energy Research* 29 (2022).

[9] Haysom, J. E., Jafarieh, O., Anis, H., Hinzer, K. and Wright, D. "Learning curve analysis of concentrated photovoltaic systems". *Progress in Photovoltaics: Research and Applications* 23.11, 2014, pp. 1678–1686.

[10] Fraunhofer Institute for Solar Energy Systems ISE. *"Current status of concentrator photovoltaic (CPV) technology"*. URL: https://www.ise.fraunhofer.de/content/dam/ise/de/documents/publications/studies/cpv-report-ise-nrel.pdf (visited on 12/14/2022).

[11] ASTM International. *"ASTM E927-19 Standard Classification for Solar Simulators for Electrical Performance Testing of Photovoltaic Devices"*. URL: https://www.astm.org/e0927-19.html (visited on 11/24/2022).

[12] ASTM International. *"ASTM G173-03(2020) Standard Tables for Reference Solar Spectral Irradiances: Direct Normal and Hemispherical on 37° Tilted Surface"*. URL: https://www.astm.org/Standards/G173.htm (visited on 11/24/2022).

[13] ASTM International. *"ASTM E490-22: Standard Solar Constant and Zero Air Mass Solar Spectral Irradiance Tables"*. URL: https://www.astm.org/e0490-22.html (visited on 11/24/2022).

[14] Gueymard, C. A. "Solar Radiation Spectrum". *Solar Energy*. Springer New York, 2013.

[15] Gombosi, T. I. *"Physics of the Space Environment"*. Cambridge University Press, 1998.

[16] Muneer, T., Gueymard, C. and Kambezidis, H. *"Solar Radiation and Daylight Models : For the Energy Efficient Design of Buildings"*. Jordan Hill: Taylor Francis Group, 2004.

[17] Gray, J.L. "The Physics of the Solar Cell". *Handbook of Photovoltaic Science and Engineering*. Ed. by A. Luque and S. Hegedus. John Wiley & Sons, 2011.

[18] Nijegorodov, N. and Luhanga, P. "Air mass: Analytical and empirical treatment; an improved formula for air mass". *Renewable Energy* 7.3, 1996, pp. 57–65.

[19] National Renewable Energy Laboratory. *"NSRDB: National Solar Radiation Database"*. URL: https://nsrdb.nrel.gov/data-sets/us-data (visited on 11/24/2022).

[20] Emery, Keith. "Measurement and Characterization of Solar Cells and Modules". *Handbook of Photovoltaic Science and Engineering*. Ed. by A. Luque and S. Hegedus. John Wiley & Sons, 2011.

[21] Badescu, V. *"Modeling Solar Radiation at the Earth's Surface: Recent Advances"*. Springer Berlin / Heidelberg, 2008.

[22] Salby, M. L. *"Physics of the Atmosphere and Climate"*. 2nd ed. Cambridge University Press, 2012.

[23] Goody, R. M. and Yung, Y. L. *"Atmospheric Radiation: Theoretical Basis"*. Oxford University Press, 2020.

[24] Degheidy, A., Sallah, M., Elgarayhi, A. and Shaaban, S. "Optical and radiative-transfer properties of mixed atmospheric aerosols". *Advances in Space Research* 55.7 (2015), 1832–1844.

[25] Masoom, A., Kashyap, Y. and Bansal, A. "Solar Radiation Assessment and Forecasting Using Satellite Data". *Advances in Solar Energy Research*. Ed. by H. Tyagi, A. K. Agarwal, P. R. Chakraborty and S. Powar. Singapore: Springer Singapore, 2019, 45–71.

[26] Liang, S., Wang, K., Zhang, X. and Wild, M. "Review on Estimation of Land Surface Radiation and Energy Budgets From Ground Measurement, Remote Sensing and Model Simulations". *IEEE Journal of Selected Topics in Applied Earth Observations and Remote Sensing* 3.3 (2010), 225–240.

[27] Gueymard, C. A. "Clear-sky irradiance predictions for solar resource mapping and large-scale applications: Improved validation methodology and detailed performance analysis of 18 broadband radiative models". *Solar Energy* 86.8 (2012), 2145–2169.

[28] Emde, C., Buras-Schnell, R., Kylling, A., Mayer, B., Gasteiger, J., Hamann, U., Kylling, J., Richter, B., Pause, C., Dowling, T. and Bugliaro, L. "The libRadtran

software package for radiative transfer calculations (version 2.0.1)". *Geoscientific Model Development* 9.5 (2016).

[29] Esen, V., Sağlam, Ş. and Oral, B. "Light sources of solar simulators for photovoltaic devices: A review". *Renewable and Sustainable Energy Reviews* 77 (2017).

[30] OAI. *"TriSOL™ CPV Solar Simulators"*. URL: https://oainet.com/product/trisol-cpv-solar-simulators/ (visited on 11/27/2022).

[31] G2V Optics Inc. *"Pico™ Small Area LED Solar Simulator"*. URL: https://g2voptics.com/products/pico-solar-simulator/ (visited on 11/27/2022).

[32] Dimitrijev, S. *"Principles of Semiconductor Devices"*. Oxford University Press, 2012.

[33] Bhattacharya, D. and Sharma, R. *"Solid State Electronic Devices"*. Oxford University Press, 2013.

[34] Kitai, A. *"Principles of solar cells, LEDs and diodes: the role of the PN junction"*. Wiley, 2011.

[35] Friedman, D., Olson, J. and Kurtz, S. "High-Efficiency III-V Multijunction Solar Cells". *Handbook of Photovoltaic Science and Engineering*. Ed. by A. Luque and S. Hegedus. John Wiley & Sons, 2011.

[36] Tampere University, Optoelectronics Research Centre. *"AMETIST - The Photovoltaics of Tomorrow"*. URL: https://projects.tuni.fi/ametist/about/ (visited on 11/25/2022).

[37] Geisz, J. F., France, R. M., Schulte, K. L., Steiner, M. A. and Norman, A. G. e. a. "Six-junction III–V solar cells with 47.1% conversion efficiency under 143 Suns concentration". *Nature Energy* 5 (2020).

[38] Vos, A. D. "Detailed balance limit of the efficiency of tandem solar cells". *Journal of Physics D: Applied Physics* 13.5 (1980).

[39] The National Renewable Energy Laboratory. *"Photovoltaic Research: Best Research-Cell Efficiency Chart"*. URL: https://www.nrel.gov/pv/cell-efficiency.html (visited on 12/15/2022).

[40] Deen, M. J. and Basu, P. K. *"Silicon Photonics: Fundamentals and Devices"*. John Wiley Sons, Incorporated, 2012.

[41] Kylling, A. and Mayer, B. "The libRadtran Software Package for Radiative Transfer Calculations - Description and Examples of Use". *Atmospheric Chemistry and Physics* 5.7 (2005).

[42] Anderson, G., Clough, S., Kneizys, F., Chetwynd, J. and Shettle, E. "AFGL atmospheric constituent profiles (0-120 km)". *Tech. Rep. AFGL-TR-86-0110*. US Air Force Geophysics Laboratory, 1986.

[43] European Centre for Medium-Range Weather Forecasts. *"ERA5 hourly data on single levels from 1959 to present"*. URL: https://cds.climate.copernicus.eu/cdsapp#!/dataset/reanalysis-era5-single-levels?tab=overview (visited on 11/27/2022).

[44] National Aeronautics and Space Administration. *"Aura Validation Data Center"*. URL: https://avdc.gsfc.nasa.gov/index.php?site=1436084398 (visited on 11/27/2022).

[45] Isoaho, R., Aho, A., Tukiainen, A. and Guina, M. "Temperature dependent characteristics of GaInP/GaAs/GaInNAsSb solar cell under simulated AM0 spectra". *2017 IEEE 44th Photovoltaic Specialist Conference (PVSC)*. 2017, 2520–2523.

[46] Aho, A., Isoaho, R., Tukiainen, A., Polojärvi, V., Raappana, M., Aho, T. and Guina, M. "Performance of Dilute Nitride Triple Junction Space Solar Cell Grown by MBE". *E3S Web Conf.* 16 (2017), 03008.

[47] Khan, T. Q., Bodrogi, P., Vinh, Q. T. and Winkler, H. *"LED Lighting: Technology and Perception"*. 1st ed. John Wiley Sons, Incorporated, 2015.

A SIMULATED LOCAL SOLAR SPECTRA

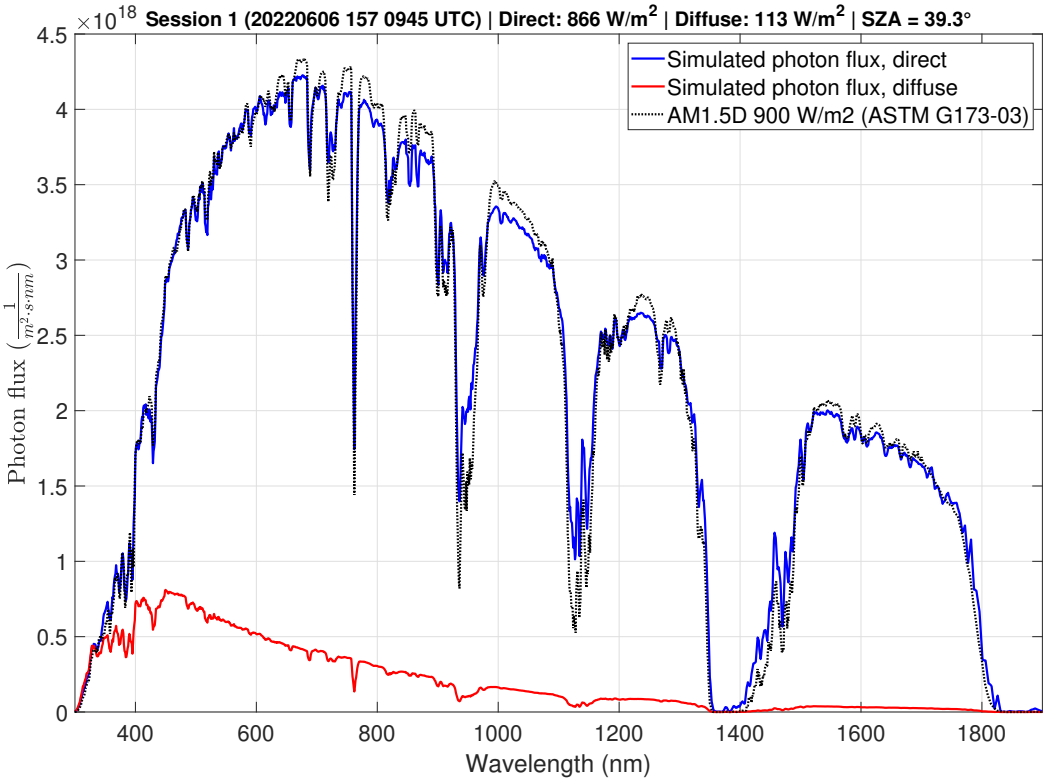

Figure A.1. *Simulated photon flux spectrum for Session 1.*

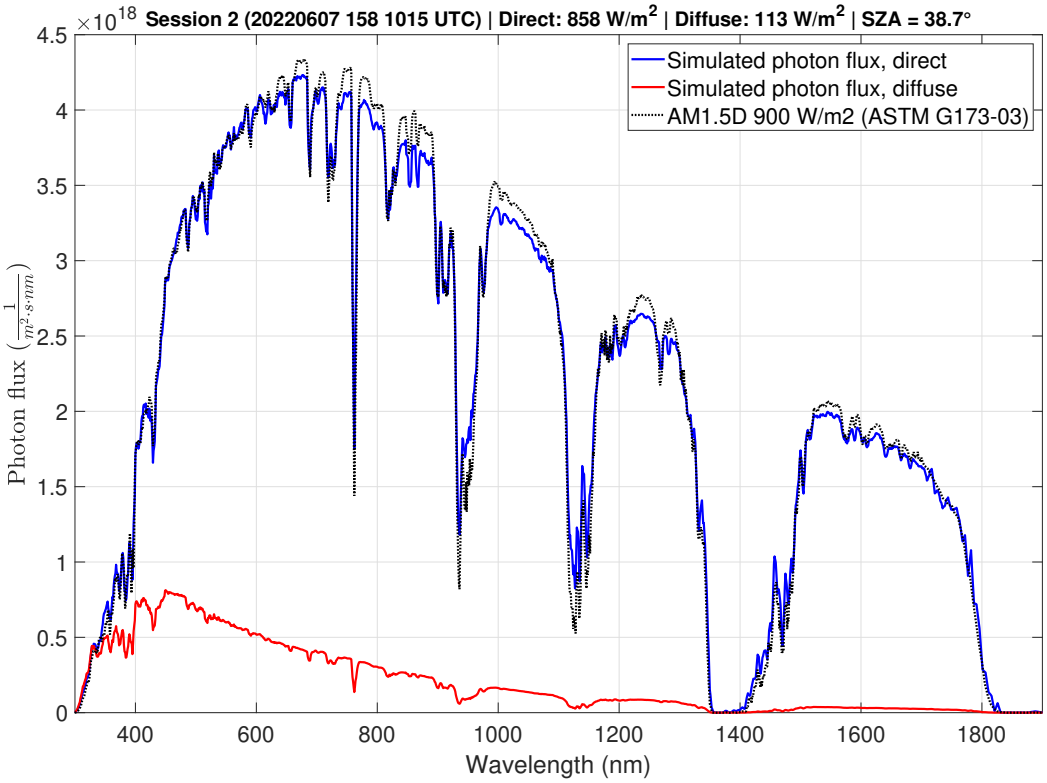

Figure A.2. *Simulated photon flux spectrum for Session 2.*

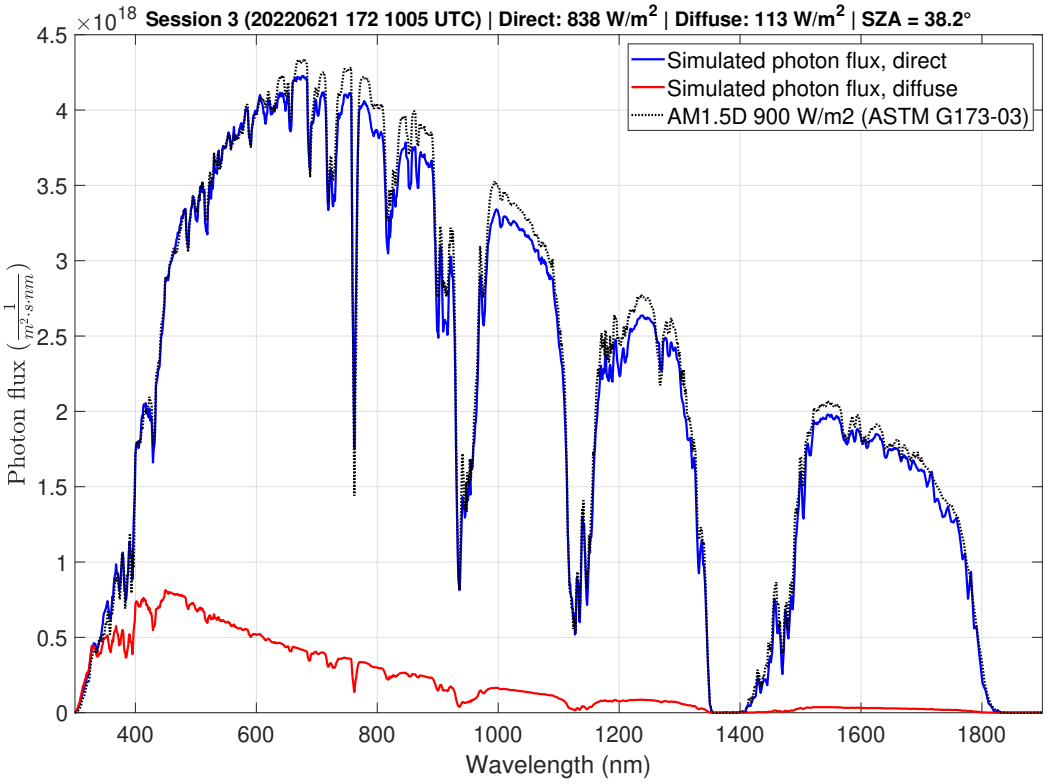

Figure A.3. *Simulated photon flux spectrum for Session 3.*

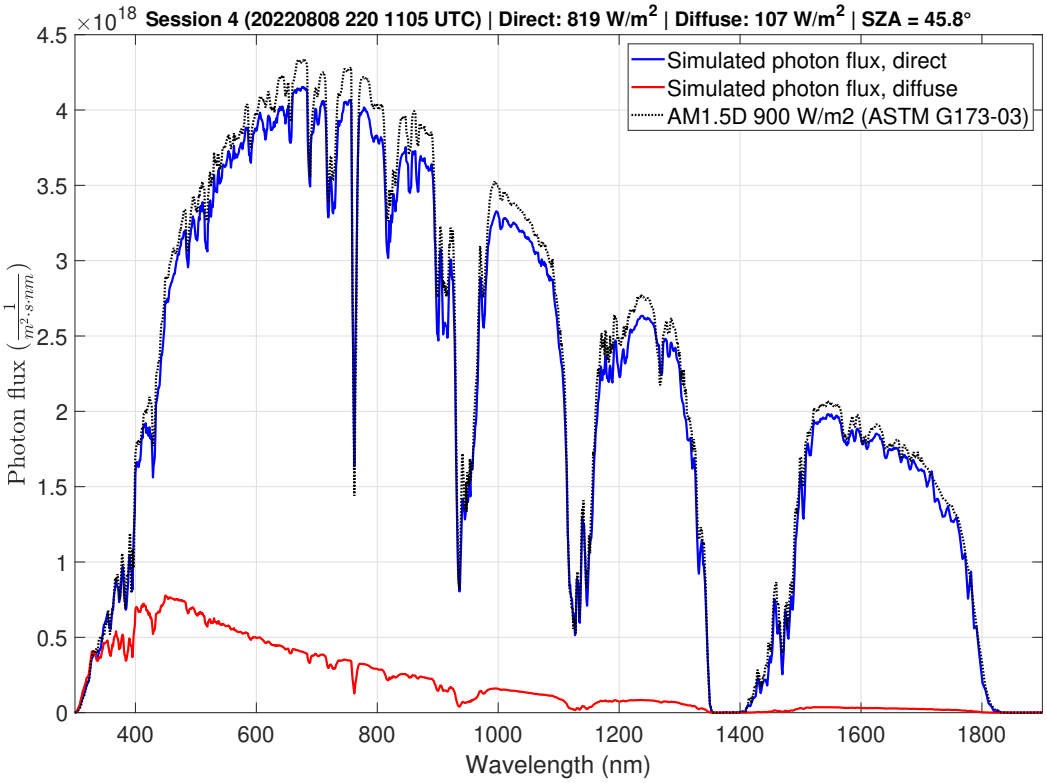

Figure A.4. *Simulated photon flux spectrum for Session 4.*

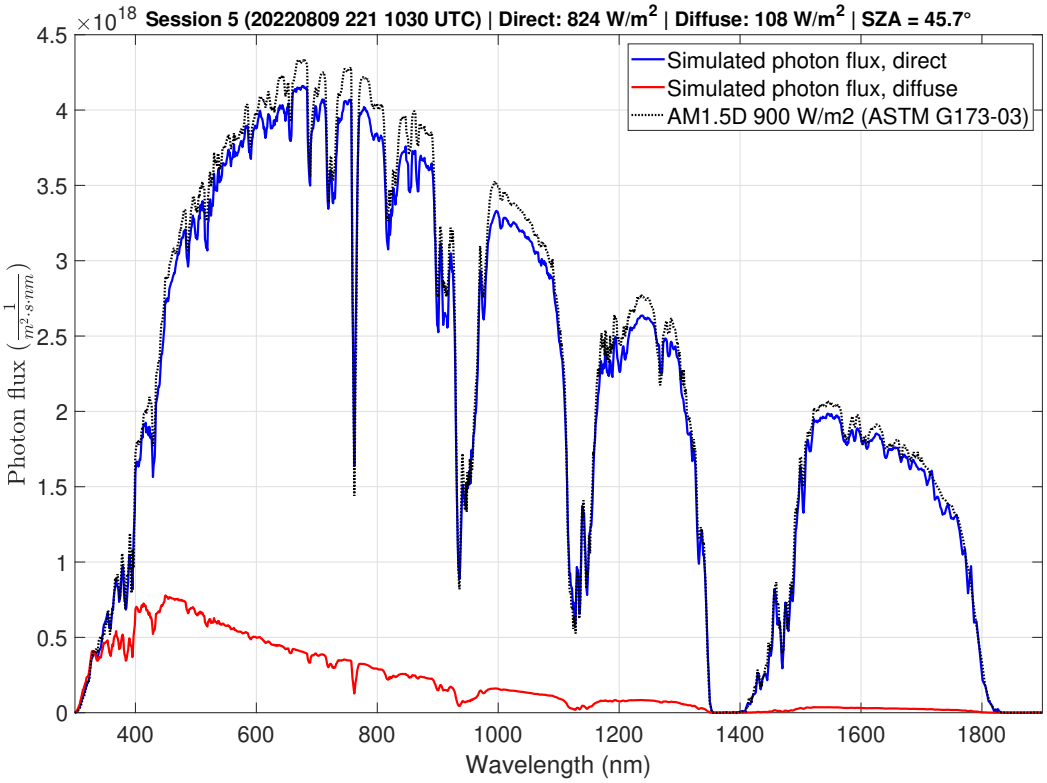

Figure A.5. *Simulated photon flux spectrum for Session 5.*

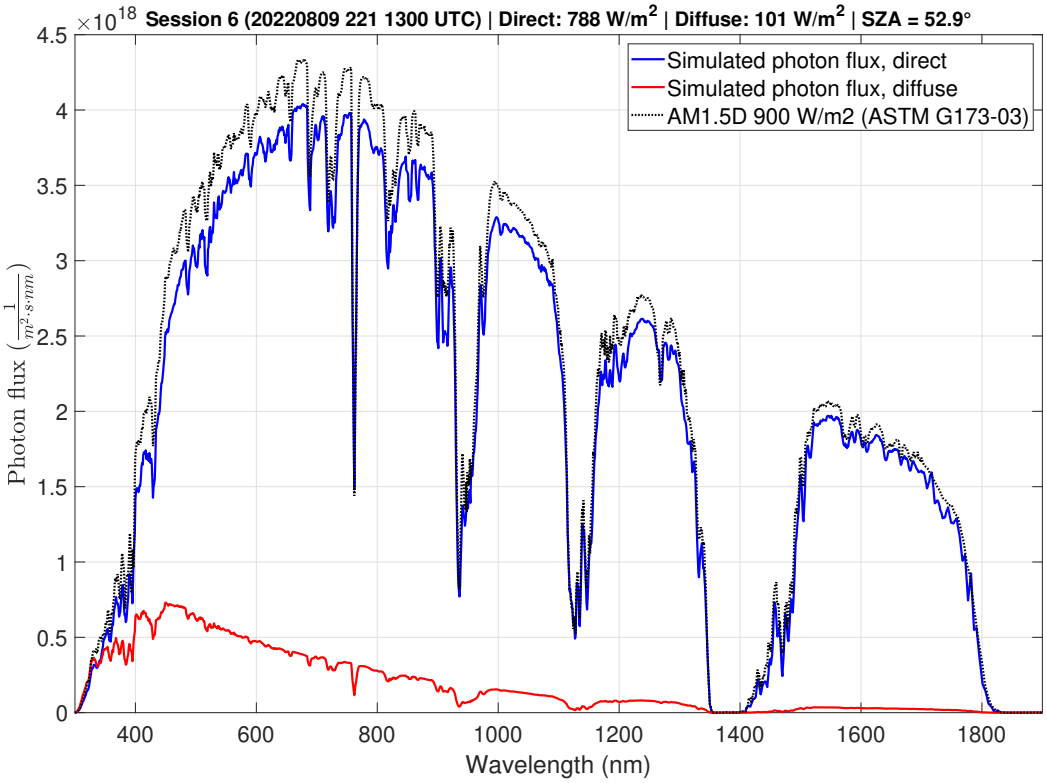

Figure A.6. *Simulated photon flux spectrum for Session 6.*

B CALIBRATION CURRENT DENSITY GRAPHS

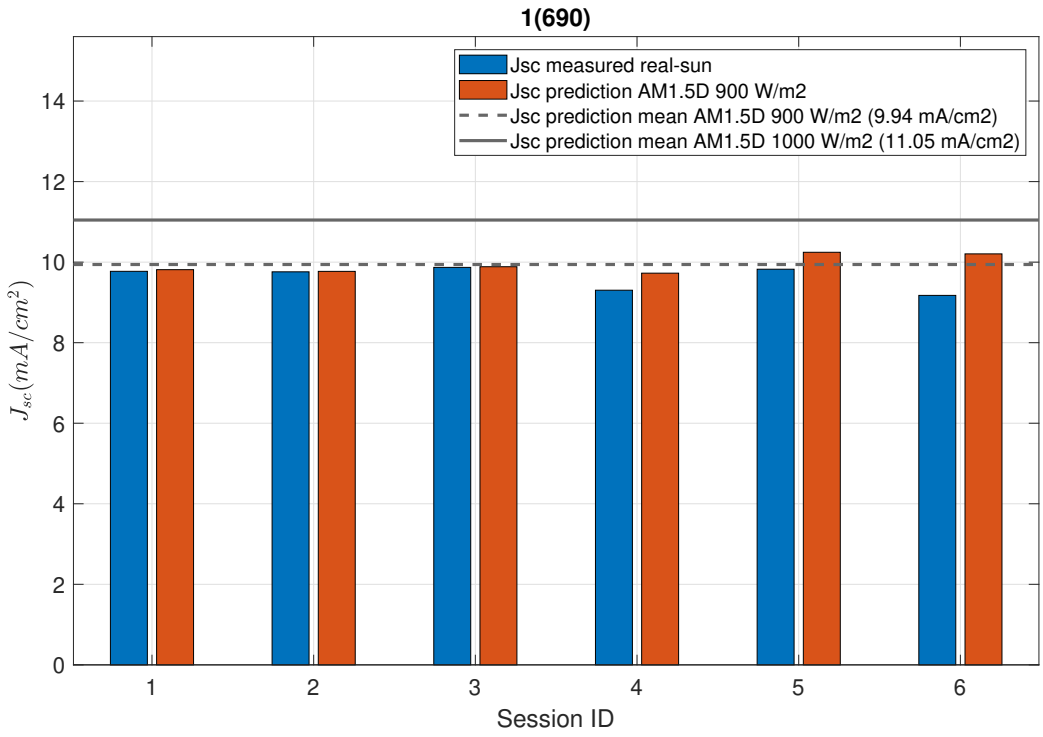

Figure B.1. *Summary of calibration currents for sample 1(690) with FS window on top. Calibration target AM1.5D (ASTM G173-03 [12]).*

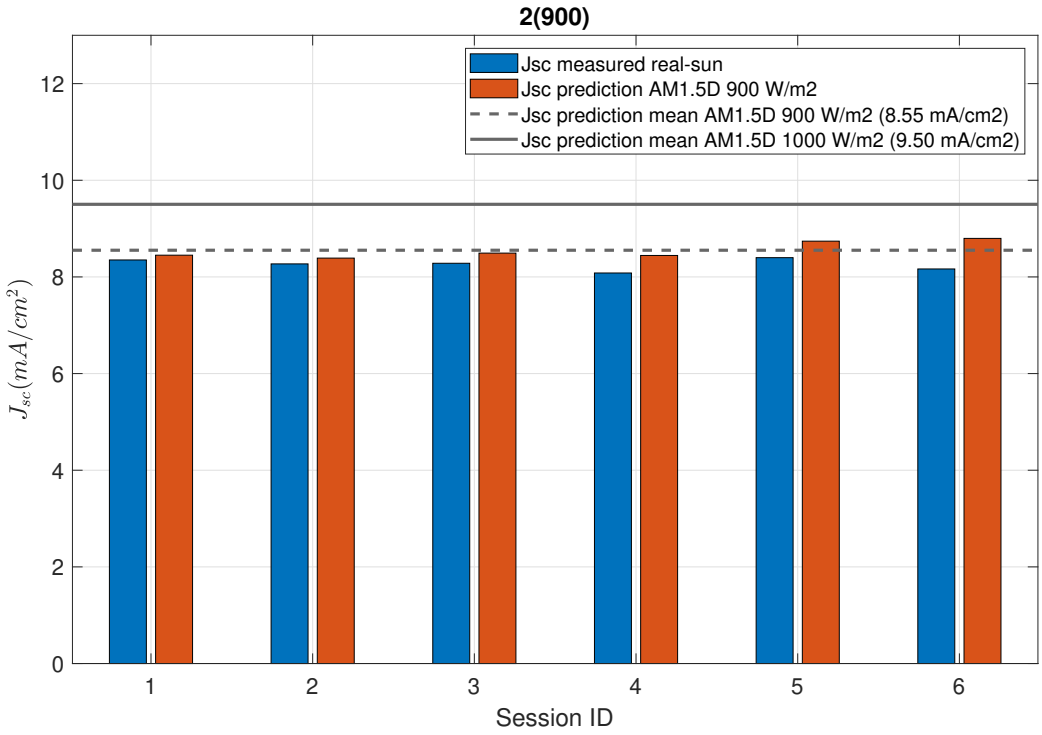

Figure B.2. *Summary of calibration currents for sample 2(900) with FS window on top. Calibration target AM1.5D (ASTM G173-03 [12]).*

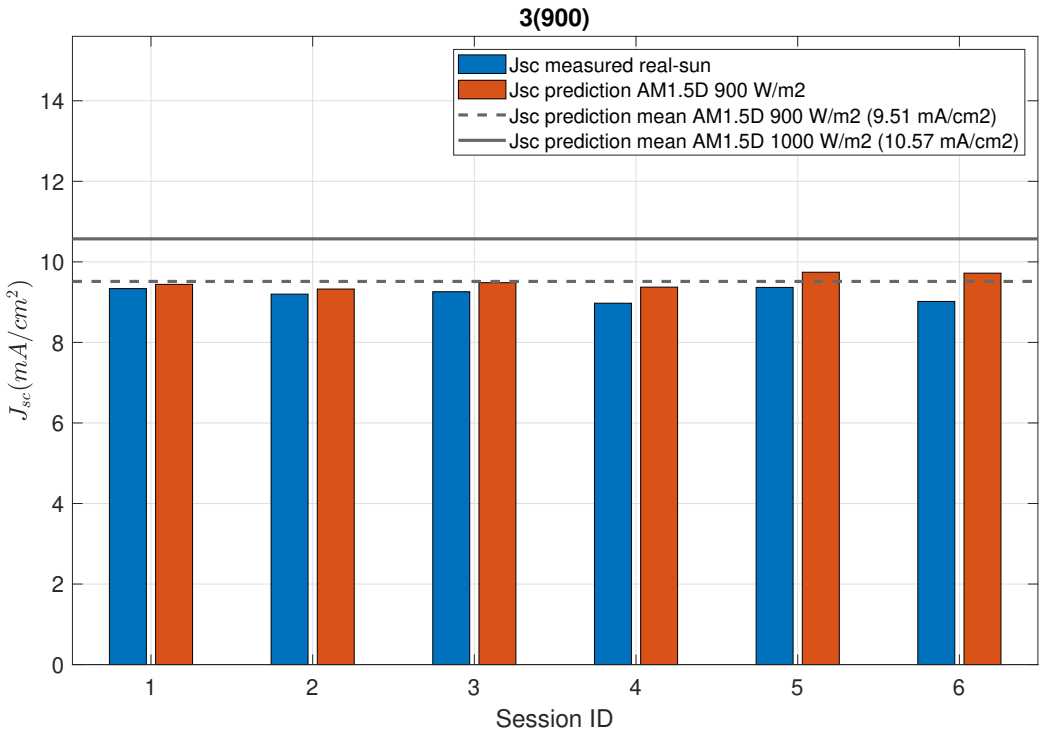

Figure B.3. *Summary of calibration currents for sample 3(900) with FS window on top. Calibration target AM1.5D (ASTM G173-03 [12]).*

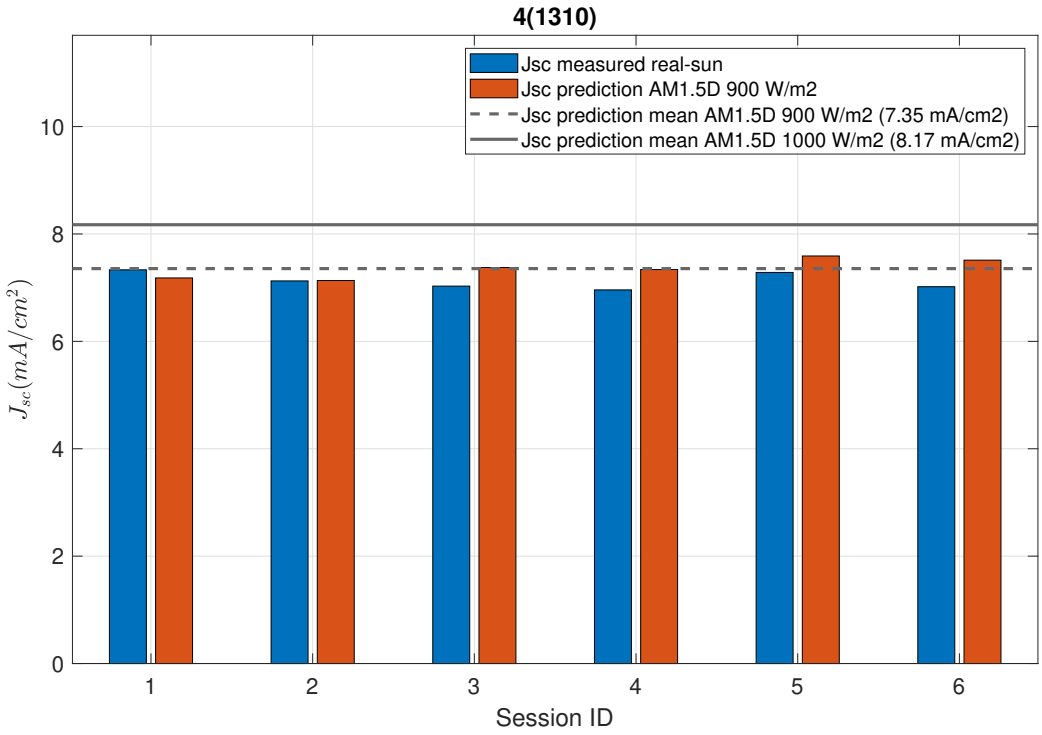

Figure B.4. *Summary of calibration currents for sample 4(1310) with FS window on top. Calibration target AM1.5D (ASTM G173-03 [12]).*

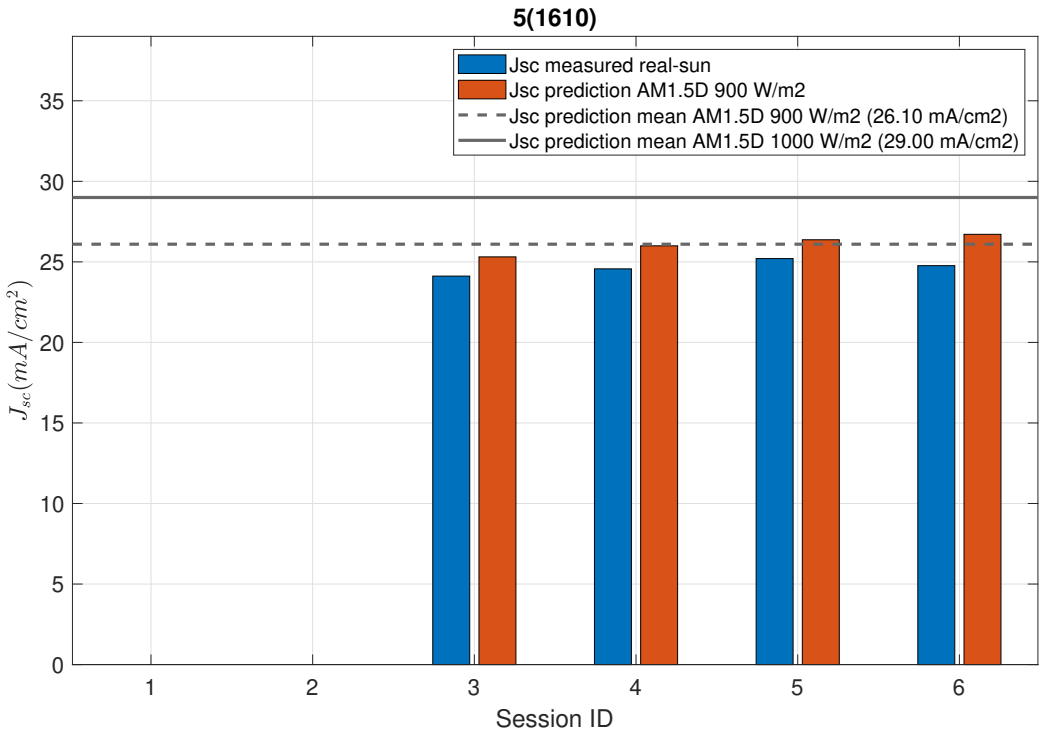

Figure B.5. *Summary of calibration currents for sample 5(1610) with FS window on top. Calibration target AM1.5D (ASTM G173-03 [12]).*

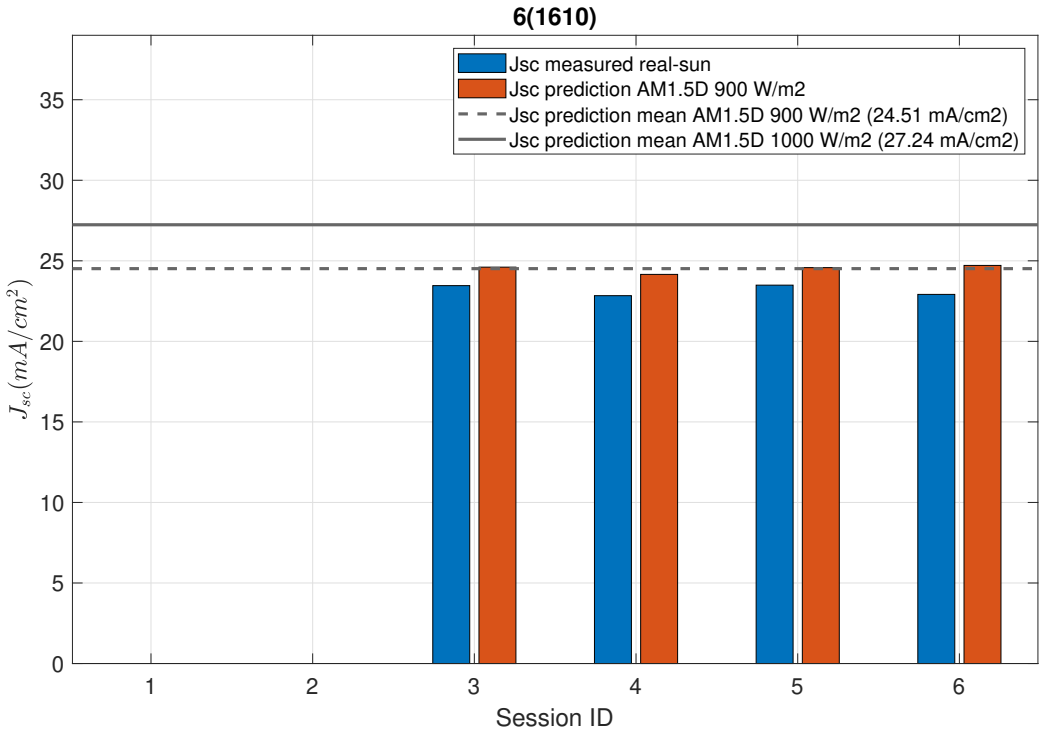

Figure B.6. *Summary of calibration currents for sample 6(1610) with FS window on top. Calibration target AM1.5D (ASTM G173-03 [12]).*